

# Characteristic time and length scales in melts of Kremer-Grest bead-spring polymers with wormlike bending stiffness

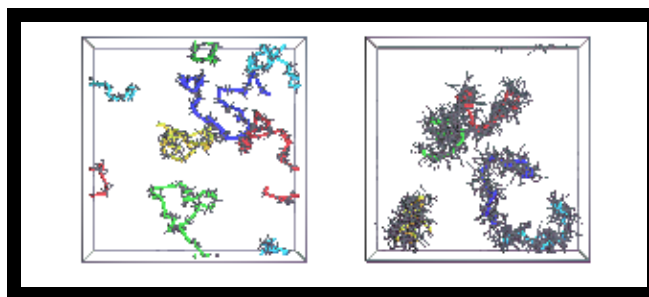
Carsten Svaneborg<sup>\*,†</sup> and Ralf Everaers<sup>‡</sup>

<sup>†</sup>*University of Southern Denmark, Campusvej 55, DK-5230 Odense M, Denmark*

<sup>‡</sup>*Univ Lyon, ENS de Lyon, Univ Claude Bernard, CNRS, Laboratoire de Physique and  
Centre Blaise Pascal, F-69342 Lyon, France*

E-mail: science@zqex.dk

## Table of content graphic



## Abstract

The Kremer-Grest (KG) model is a standard for studying generic polymer properties. Here we have equilibrated KG melts up to and beyond 200 entanglements per chain for varying chain stiffness. We present methods for estimating the Kuhn length corrected for incompressibility effects, for estimating the entanglement length corrected for chain stiffness, for estimating bead frictions and Kuhn times taking into account entanglement effects. These are the key parameters for enabling quantitative, accurate, and parameter free comparisons between theory, experiment and simulations of KG polymer models with varying stiffness. We demonstrate this for the mean-square monomer displacements in moderately to highly entangled melts as well as for the shear relaxation modulus for unentangled melts, which are found to be in excellent agreement with the predictions from standard theories of polymer dynamics.

## 1 Introduction

Polymeric materials share universal properties,<sup>1-6</sup> which depend on atomistic details only through a small number of interrelated characteristic time and length scales and which vary in a characteristic manner with the contour length,  $L$ , the molecular weight,  $M \sim L$ , or the number of monomers,  $N \sim M \sim L$ , of linear chains.<sup>1-6</sup> For example, the mean-square end-to-end distance in a melt varies like,  $\langle R^2 \rangle = l_K L$ , as chains with a contour length exceeding the Kuhn<sup>7</sup> length,  $l_K$ , adopt random walk conformations.<sup>8</sup>

Analytical theory<sup>1-6</sup> distills understanding of the complex emergent behavior in terms of simplifying phenomenological models of the large scale conformational statistics and dynamics of densely packed, interpenetrating, random walk-like chains. Computer simulations<sup>9-15</sup> play an increasingly important, complementary role by providing insight<sup>16</sup> and by validating phenomenological theories<sup>17</sup> for well-defined model systems. Here we are interested in the standard Molecular Dynamics (MD) model for simulating the structure and dynamics of polymer melts, the bead-spring model of Kremer and Grest (KG).<sup>18,19</sup> In the KG model

approximately hard sphere beads are connected by strong non-linear springs, generating the connectivity and the liquid-like monomer packing characteristic of polymer melts. The model is formulated in terms of the microscopic energy scale,  $\epsilon$ , bead diameter,  $\sigma$ , mass,  $m_b$ , and time  $\tau = \sigma\sqrt{m_b/\epsilon}$  of the Lennard-Jones interactions between the beads. The parameters are tuned to energetically prevent polymer chains from passing through each other. Since the model reproduces the local topological constraints, which dominate the dynamics of long-chain polymers,<sup>19</sup> non-trivial large scale entanglement properties *emerge* through the exact same mechanisms as in real polymer melts. The KG model was devised to study the generic properties of polymers with an emphasis on simplicity and computational efficiency. It has been used to investigate the effects of polymer entanglements, branching, chain polydispersity, and/or chemical cross-linking, see Refs.<sup>20–27</sup> for examples. The utility of generic models is not limited to bulk materials. KG-like models have also been used to study universal aspects of the behaviour of tethered and spatially confined polymers, of welding of polymer interfaces or of composite materials formed by adding filler particles to a polymer melt or solid, see Refs.<sup>28–37</sup> for examples.

Here we present an accurate characterization and parameterization of the key characteristic time and length scales of the KG model: the Kuhn length,  $l_K$ , the number of Kuhn segments,  $N_{eK}$ , between entanglements, the Kuhn segmental friction,  $\zeta_K$  and the associated Kuhn time,  $\tau_K$ , and entanglement time  $\tau_e$ . In particular, we study their variation with the strength of an additional bending potential introduced by Faller and Müller-Plathe.<sup>38–40</sup> Our results are based on the analysis of well equilibrated melts of KG chains of varying stiffness, which cover the entire range from unentangled to highly entangled systems with up to and beyond  $Z = 200$  entanglements per chain. They allow us to address three different types of questions:

1. With respect to the KG model itself, we seek to establish and better understand how the additional bending term affects the emergent length and time scales. This is similar to the experimental interest in carefully characterizing suitable reference systems or

families of chemically similar systems with tunable microscopic structure<sup>41,42</sup> to allow for systematic experimental studies of structure-property relations.

2. With respect to experiment, a follow-up article<sup>43</sup> introduces “Kuhn scale-mapped KG models” as minimal material-specific polymer models by matching (i) the Kuhn number,  $n_K = \rho_K l_K^3$ , as a dimensionless measure of density and (ii) the number of Kuhn segments per chain,  $N_K$ , as a dimensionless measure of chain length. We show that the family of models investigated here covers the full range relevant for melts of commodity polymers. The standard KG model maps onto the intrinsically most flexible experimental systems (PDMS and poly-isoprene), which are characterized by the smallest Kuhn number. These systems come closest to the theoretical ideal of an infinite number of Kuhn segments,  $N_{eK}$ , between entanglements. Melts of stiffer polymers like poly-ethylene or poly-carbonate have higher Kuhn numbers and only a finite number of Kuhn segments per entanglement length. Corresponding Kuhn scale-mapped KG models account for this effect and can be expected to reproduce deviations from idealised theoretical predictions. As a simple example, the reader may think of the finite maximal elongation of entanglement segments.

3. With respect to polymer theory, we note that expressions for experimental observables are usually formulated in units defined by the relevant time and length scales in combination with  $k_B T$  as the typical energy scale for entropy dominated phenomena. Knowledge of these fundamental scales thus puts us in a position to carry out parameter-*free* tests of theoretical predictions for a wide and representative range of generic polymer models. Theoretical predictions are often derived for limiting cases. Deviations (such as static and dynamic effects due to chain stiffness, finite number of Kuhn segments between entanglements, incompressibility, as well as end and entanglement effects on chain friction) observed for the present model systems do *not* constitute artifacts of an arbitrarily defined computational polymer model. Given the

mapping to experimental systems they should rather be thought of as representative for real polymers.

The paper is structured as follows. In Sec. 2 we introduce the Kremer-Grest model and provide the necessary theoretical background: we (i) define the targeted characteristic time and length scales, (ii) relate them to computational observables and (iii) discuss corrections to the ideal behavior assumed in their definition. Section 3 presents the methods we use to set up and simulate our systems and to analyze the raw data. For example, our estimator for the Kuhn length accounts for long-range correlations induced by the melt incompressibility<sup>44,45</sup> and our PPA<sup>16</sup> estimator for the entanglement length<sup>46</sup> takes into account the finite number of Kuhn segments per entanglement. A key point is our strategy to estimate the effective bead friction, which uses theoretical guidance to disentangle the influence of end effects,<sup>47–50</sup> inertia, local chain stiffness, the correlation hole,<sup>51</sup> viscoelastic hydrodynamic interactions,<sup>52–54</sup> and entanglements.<sup>4</sup> In Sec. 4 we present our results. In particular, we extract the Kuhn and entanglement lengths as well as the effective bead friction in KG melts. In the following Discussion in Sec. 5, we derive and discuss the corresponding Kuhn and entanglement times. The phenomenological interpolations for the stiffness dependence of the Kuhn length,  $l_K$ , the Kuhn friction,  $\zeta_K$ , the Kuhn time,  $\tau_K$ , the entanglement length,  $N_{eK}$ , and the entanglement time,  $\tau_e$  form the basis of our parameterization of “Kuhn scale-mapped KG models” in the accompanying paper.<sup>43</sup> Here we focus on the third point of the above list and present *parameter-free* comparisons between our data and the predictions of the Rouse and tube models of polymer melts. The two models work remarkably well on scales, where KG chains can be described as Gaussian chains. On smaller scales, the Rouse model describes the dynamics of unentangled chains only qualitatively. Deviations become more pronounced for stiffer chains, as the gap between the Kuhn and the entanglement scales closes rapidly with increasing bending rigidity. In the final Sec. 6, we summarise and present our conclusions.

## 2 Model and background

Polymeric materials share universal properties, which depend on atomistic details only through a small number of interrelated characteristic time and length scales. In the following we present and define these scales together with the Kremer-Grest (KG) model. The material is essentially standard with the exception of the phantom KG simulations (Sec. 2.4) and the *definition* of the Kuhn time,  $\tau_K$ , based on the Rouse model (Sec. 2.5). A detailed discussion of our estimators for the various time and length scales can be found in the following Methods section.

### 2.1 The Kremer Grest Model

The KG model<sup>18,19</sup> is a bead-spring model, where the mutual interactions between all beads are given by the truncated Lennard-Jones or Weeks-Chandler-Anderson (WCA) potential,

$$U_{WCA}(r) = 4\epsilon \left[ \left(\frac{\sigma}{r}\right)^{-12} - \left(\frac{\sigma}{r}\right)^{-6} + \frac{1}{4} \right] \quad \text{for } r < 2^{1/6}\sigma, \quad (1)$$

where  $\epsilon = k_B T$  and  $\sigma$  are chosen as the simulation units of energy and distance, respectively. Bonded beads additionally interact through the finite-extensible-non-linear elastic spring (FENE) potential,

$$U_{FENE}(r) = -\frac{kR^2}{2} \ln \left[ 1 - \left(\frac{r}{R}\right)^2 \right]. \quad (2)$$

We adopt the standard choices for the Kremer-Grest model of  $R = 1.5\sigma$  for the maximal bond length,  $k = 30\epsilon\sigma^{-2}$  for the spring constant, and  $\rho_b = 0.85\sigma^{-3}$  for the bead density. Here and below we use subscript “b” to denote bead specific properties to distinguish these from Kuhn units. Following Faller and Müller-Plathe<sup>38–40</sup> we add an entropic “wormlike”<sup>55</sup> bending potential defined by

$$U_{bend}(\Theta) = \kappa k_B T (1 - \cos \Theta), \quad (3)$$

where  $\Theta$  denotes the angle between subsequent bonds and  $\kappa$  is a dimensionless bending stiffness. Temperature-independent bending potentials of this form are routinely used to model semi-flexible polymers. For other possible choices of bending potentials, see e.g. Ref.<sup>56</sup> The average bond length is  $l_b = 0.965\sigma$ , so that the contour length of a linear chain composed of  $N_b$  beads is given by  $L = (N_b - 1)l_b$ . The variation of 0.2% of the bond length over the considered  $\kappa$ -range is so small, that we may neglect the effect for the present purposes. The WCA interactions between next-nearest beads define a maximum bending angle between subsequent bonds. In simulations with negative  $\kappa$  this effect is partially compensated, resulting in KG melts that are somewhat more flexible than the standard KG model.

As in the original KG papers,<sup>18,19</sup> we integrate Langevin equations of motion

$$m_b \frac{\partial^2 \mathbf{R}_i}{\partial t^2} = -\nabla_{\mathbf{R}_i} U - \Gamma \frac{\partial \mathbf{R}_i}{\partial t} + \boldsymbol{\xi}_i(t) \quad (4)$$

where  $\mathbf{R}_i$  denotes the position of bead  $i$  and  $U$  the total potential energy.  $\boldsymbol{\xi}_i(t)$  is a Gaussian distributed random vector with  $\langle \boldsymbol{\xi}_i(t) \rangle = 0$  and  $\langle \boldsymbol{\xi}_i(t) \cdot \boldsymbol{\xi}_j(t') \rangle = 6\Gamma k_B T \delta(t - t') \delta_{ij}$ . The mass of a bead is denoted  $m_b$ , and we choose this as our mass scale for the simulations. From the units defined so far, follows that time in KG simulations is measured in units of  $\tau = \sigma \sqrt{m_b / \epsilon}$ .

## 2.2 Large scale structure and Kuhn length

The most important measure of the overall chain size is the mean-square end-to-end distance,  $\langle R^2 \rangle$ . For many polymeric systems, it varies in a characteristic manner,  $\langle R^2 \rangle \sim L^{2\nu} \sim M^{2\nu} \sim N^{2\nu}$ , with the contour length,  $L$ , the molecular weight,  $M$ , the number of monomers,  $N$ , or any other measure of the length of linear chains.<sup>1-6</sup> In the melt state, polymers adopt random walk conformations<sup>8</sup> with  $\nu = 1/2$ . In this case, the gyration radius is given by  $\langle R_g^2 \rangle = \langle R^2 \rangle / 6$ .

For chains characterized by  $\nu = 1/2$ , the Kuhn length,<sup>7</sup>  $l_K$ , is defined by a mapping to a freely-jointed chain model composed of  $N_K$  Kuhn steps, which reproduces the mean-square end-to-end distance and the end-to-end distance at full extension,

$$\langle R^2 \rangle = l_K^2 N_K \quad (5)$$

$$L = l_K N_K, \quad (6)$$

of the target polymers. Beyond the Kuhn scale the behavior of polymer chains is dominated by thermal fluctuations and is *universal*.<sup>3-5</sup> Below the Kuhn scale chains are rigid,  $\langle R^2 \rangle \propto L^2$ . Their behavior is material specific and dependent on atomic details. Given  $l_K$ , it is straightforward to obtain the number of Kuhn segments per chain,  $N_K = \langle R^2 \rangle / l_K^2 = L^2 / \langle R^2 \rangle$ . The number density of Kuhn segments is  $\rho_K = N_K \rho_c$  where  $\rho_c$  denotes the number density of chains.

For freely rotating (bead-spring) chains with the bending potential, Eq. (3), the bare Kuhn length in the absence of excluded volume interactions is given by:<sup>2,57</sup>

$$l_K = l_b \frac{1 + \langle \cos(\theta) \rangle}{1 - \langle \cos(\theta) \rangle} \quad (7)$$

$$l_K^{(0)}(\kappa) = l_b \times \begin{cases} \frac{2\kappa + e^{-2\kappa} - 1}{1 - e^{-2\kappa}(2\kappa + 1)} & \text{if } \kappa \neq 0 \\ 1 & \text{if } \kappa = 0 \end{cases} \quad (8)$$

The Kratky-Porod wormlike chain expression:<sup>55</sup>

$$\frac{\langle R^2(N_K) \rangle}{l_K^2 N_K} = 1 - \frac{1}{2N_K} (1 - e^{-2N_K}), \quad (9)$$

provides a convenient interpolation between the rigid rod and random walk limits. For chains following random walk statistics on larges scales, equations (5) and (6) suggests to define



the Kuhn length as

$$l_K = \lim_{L \rightarrow \infty} \frac{\langle R^2 \rangle}{L}. \quad (10)$$

Note, however, that  $l_K$  can in general not be estimated by fitting Eq. (9) to (simulation) data for chains in a melt, since this expression neglects long-range bond orientation correlations due to the incomplete screening of excluded volume interactions.<sup>44,45,58–60</sup> (see Sec. 3.3 for a more detailed discussion).

### 2.3 Langevin dynamics

The standard theory of polymer dynamics in the melt state<sup>4</sup> describes the coarse-grain chain motion through an overdamped *single-chain* Langevin equation,

$$0 = -\nabla_{\mathbf{R}_i} \tilde{\mathcal{H}} - \frac{\zeta_{cm}}{N} \frac{\partial \mathbf{R}_i}{\partial t} + \boldsymbol{\xi}_i(t). \quad (11)$$

for the retained  $N$  spatial degrees of freedom,  $\mathbf{R}_i$ .  $\tilde{\mathcal{H}}$  denotes a corresponding effective single-chain Hamiltonian to be inferred from the chain statistics in the fully interacting system, i.e. the potential of mean force felt by a chain.<sup>61</sup> Eq. (11) implies a constant effective friction  $\zeta_{cm}/N$  per bead.  $\boldsymbol{\xi}_i(t)$  are normally distributed random vectors with statistics characterized by  $\langle \boldsymbol{\xi}_i(t) \rangle = 0$  and  $\langle \boldsymbol{\xi}_i(t) \cdot \boldsymbol{\xi}_j(t') \rangle = 6 \frac{\zeta_{cm}}{N} k_B T \delta(t - t') \delta_{ij}$ . Within this description, the chain centers-of-mass  $\mathbf{R}_{cm}(t)$  exhibit simple diffusion,

$$\lim_{t \rightarrow \infty} \langle (\mathbf{R}_{cm}(t) - \mathbf{R}_{cm}(0))^2 \rangle \equiv \lim_{t \rightarrow \infty} g_3(t) = 6 D_{cm} t = 6 \frac{k_B T}{\zeta_{cm}} t, \quad (12)$$

at *all* times, i.e.  $\zeta_{cm}/N$  is the effective friction per retained degree of freedom in the fully interacting system. The largest conformational relaxation time,  $\tau_{max} \propto R_g^2/D_{cm}$ , is of the order of the time required by the chains to diffuse over a distance comparable to their size.

## 2.4 Phantom KG chains as single-chain reference model for the dynamics

In the present context, it is natural to retain the bead degrees of freedom of the target KG chains, and to study the Langevin dynamics (including the inertia term from Eq. (4)) of “phantom KG chains”:

$$m_b \frac{\partial^2 \mathbf{R}_i}{\partial t^2} = -\nabla_{\mathbf{R}_i} \tilde{\mathcal{H}} - \zeta_b \frac{\partial \mathbf{R}_i}{\partial t} + \boldsymbol{\xi}_i(t). \quad (13)$$

We define the effective Hamiltonian,  $\tilde{\mathcal{H}}$ , through the same functional form, Eqs. (1) to (3), for the bonded interactions as for the full KG model. In contrast, non-bonded intra- and interchain excluded volume interactions, which are largely screened in melts,<sup>8</sup> are neglected. The effective bending stiffness,  $\tilde{\kappa}(\kappa)$ , of the phantom KG chains is defined through the condition, that their bare Kuhn length, Eq. (8), has to reproduce the measured Kuhn lengths of the KG chains in the target melts,  $l_K^{(0)}(\tilde{\kappa}) \equiv l_K(\kappa)$ . The value of the effective bead friction,  $\zeta_b = \zeta_{cm}/N_b$ , essentially sets the time scale of the polymer motion. The crossover from the initial ballistic to the diffusive regime occurs at  $t = m_b/\zeta_b$  for both the beads and the chain CM, whose diffusion constant is given by  $D_{cm} = k_B T/\zeta_{cm}$  with  $\zeta_{cm} = \zeta_b N_b$ . In KG melts,  $\zeta_b \gg \Gamma$ , i.e. the effect of the thermostat is small compared to the friction, which arises from the interactions between the beads.<sup>19</sup> One of our tasks is to determine appropriate values of  $\zeta_b$  as a function of the stiffness parameter,  $\kappa$ .

## 2.5 Rouse dynamics

The Rouse-model<sup>62</sup> describes the Brownian dynamics, Eq. (11), beyond the Kuhn scale. Flexible polymers are described as “Gaussian” chains,

$$\tilde{\mathcal{H}} = \frac{1}{2} k_R \sum_{i=1}^{N_R} (\mathbf{R}_{i+1} - \mathbf{R}_i)^2 \quad (14)$$

composed of  $N_R + 1$  beads with  $N_R \sim L \sim M \sim N_K$ . The beads are connected by harmonic springs with spring constant  $k_R = 3N_R k_B T / \langle R^2 \rangle$ .

Rouse theory represents the internal chain dynamics in terms of a set of  $p = 1, \dots, N_R$  Rouse modes. While the Rouse model is a coarse-grain description,  $N_R \ll N_K$ , it is typically solved in the  $N_R \rightarrow \infty$  continuum limit, where each mode has a characteristic relaxation time  $\tau_p = \tau_R / p^2$ . The relaxation time of the mode with  $p = 1$  defines the Rouse time,

$$\tau_R = \frac{1}{3\pi^2} \frac{\zeta_{cm} \langle R^2 \rangle}{k_B T} \sim N_K^2. \quad (15)$$

By construction, the model reproduces the overall size,  $\langle R^2 \rangle$ , of target chains. Furthermore, within the Rouse model Eq. (12) for the CM diffusion holds at all times and can be expressed as

$$g_3(t) = \frac{2}{\pi^2} \langle R^2 \rangle \frac{t}{\tau_R}. \quad (16)$$

In particular, the Rouse model predicts sub-diffusive monomer motion,  $\delta \mathbf{R}_i(t) \equiv \mathbf{R}_i(t) - \mathbf{R}_{cm}(t)$ ,

$$g_2(t) \equiv \langle [\delta \mathbf{R}_i(t) - \delta \mathbf{R}_i(0)]^2 \rangle \quad (17)$$

$$= \frac{2}{\pi^2} \langle R^2 \rangle \sum_{p=1}^{\infty} p^{-2} \left[ 1 - \exp\left(-\frac{t}{\tau_p}\right) \right], \quad (18)$$

$$\approx \langle R^2 \rangle \begin{cases} \frac{2}{\pi^{3/2}} \sqrt{t/\tau_R} & \text{for } t \ll \tau_R \\ \frac{1}{3} & \text{for } \tau_R \gg t \end{cases}, \quad (19)$$

$g_2(t)$  measures the monomer motion relative to the CM,  $g_2(t)$ , which levels off on approaching the Rouse time,  $\tau_R$ . Beyond this time, the total monomer motion,

$$g_1(t) \equiv \langle [\mathbf{R}_i(t) - \mathbf{R}_i(0)]^2 \rangle = g_2(t) + g_3(t), \quad (20)$$

is dominated by the CM diffusion, Eq. (16).

The sub-diffusive monomer motion corresponds to an extended power-law decay of the shear relaxation modulus,

$$G_R(t) = \rho_c k_B T \sum_{p=1}^{\infty} \exp\left(-\frac{2t}{\tau_p}\right) \quad (21)$$

$$\approx k_B T \rho_c \begin{cases} \sqrt{\frac{\pi}{8}} \sqrt{\tau_R/t} & \text{for } t \ll \tau_R \\ \exp\left(-\frac{2t}{\tau_R}\right) & \text{for } \tau_R \gg t \end{cases} \quad (22)$$

which implies a macroscopic viscosity of

$$\eta_R = \int_0^{\infty} dt G_R(t) = \frac{k_B T \rho_c}{2} \sum_{p=1}^{\infty} \tau_p = \frac{\pi^2}{12} \rho_c k_B T \tau_R = \frac{1}{36} \zeta_{cm} \langle R^2 \rangle. \quad (23)$$

## 2.6 Defining Kuhn time, friction and viscosity through the Rouse model

Discretizing the chains at the Kuhn scale, the friction coefficient of Kuhn segments is given by

$$\zeta_K = \frac{\zeta_{cm}}{N_K}. \quad (24)$$

We *define* the Kuhn time (including prefactors) as

$$\tau_K \equiv \frac{1}{3\pi^2} \frac{\zeta_K l_K^2}{k_B T}, \quad (25)$$

by identifying it with the relaxation time of the  $p = N_K$  Rouse mode. Furthermore, it is convenient to define an effective viscosity at the Kuhn scale as

$$\eta_K = \frac{1}{36} \frac{\zeta_K}{l_K} \quad (26)$$

by interpreting  $\zeta_K$  as a viscous Stokes drag,  $\zeta_K \propto \eta_K l_K$ . Using these Kuhn units, the predictions of the Rouse model take the simple dimensionless form:

$$\frac{\tau_R}{\tau_K} = N_K^2 \quad (27)$$

$$\frac{\eta}{\eta_K} = n_K N_K, \quad (28)$$

where the Kuhn number,

$$n_K = \rho_K l_K^3, \quad (29)$$

is a dimensionless measure of density. A second advantage is that Kuhn units naturally indicate the validity limit of the Gaussian chain and the Rouse model for flexible polymers. Furthermore, they reveal that except for the CM motion,

$$\frac{g_3(t)}{l_K^2} = \frac{2}{\pi^2} \frac{1}{N_K} \frac{t}{\tau_K}, \quad (30)$$

the characteristic dynamics below the Rouse time is independent of chain length:

$$\frac{g_2(t)}{l_K^2} = \frac{2}{\pi^{3/2}} \sqrt{\frac{t}{\tau_K}}, \quad (31)$$

$$\frac{G_R(t) l_K^3}{k_B T} = \sqrt{\frac{\pi}{8}} n_K \sqrt{\frac{\tau_K}{t}} \quad (32)$$

## 2.7 Tube model for loosely entangled polymers

Diffusing polymers can slide past each other, but since the chain backbones cannot cross, their Brownian motion is subject to transient topological constraints, which dominate the long-time chain dynamics. Within the tube model,<sup>4,63,64</sup> the effective Hamiltonian in Eq. (11) and the corresponding static properties are thought to remain unchanged. The same holds for the isotropic short-time dynamics described by Eq. (11), while the effect of the topological constraints can be illustrated through the presence of a jungle gym-like array of obstacles.<sup>65</sup> These constraints affect the polymer dynamics beyond a characteristic entanglement (con-

tour) length or weight,  $L_e \sim M_e \sim N_e$ .<sup>4</sup> Continuing with a description at the Kuhn scale, we denote by  $N_{eK} \equiv L_e/l_k$  the number of Kuhn segments per entanglement length. For our present purposes  $N_{eK} > 1$ , i.e. the chains exhibit flexible chain behavior on the entanglement scale or “loosely entangled”.<sup>66</sup>

Within the tube model,<sup>4</sup> Eq. (11) is assumed to remain valid up to the entanglement time,  $\tau_e$ . The standard tube model<sup>4</sup> for loosely entangled polymers builds upon the Rouse model, so that

$$\tau_e = N_{eK}^2 \tau_K . \quad (33)$$

Beyond the entanglement time, chains are expected to behave as if confined to a tube<sup>64</sup> of diameter  $d_T \sim l_K N_{eK}^{1/2}$ , Kuhn length  $a_{pp} = d_T$ , and overall length  $(L/L_e)d_T \equiv Z d_T$ , which follows their coarse-grain contour. With the chain dynamics reduced to a one-dimensional diffusion within the tube (“reptation”<sup>64</sup>), full equilibration requires the chain centers of mass to diffuse over the entire length of the tube. Assuming the same effective bead friction as for the local dynamics, the terminal relaxation time is thus given by

$$\tau_d = 3Z\tau_R = 3Z^3\tau_e . \quad (34)$$

According to the tube model the monomer mean-square displacements exhibit cross-overs at the Kuhn time  $\tau_K$ , the entanglement time  $\tau_e$ , the Rouse time  $\tau_R$ , and the terminal relaxation time  $\tau_{max}$ . All regimes are characterized by a particular power laws.<sup>4</sup> The mean-square displacements in the various tube regimes can be calculated by projecting *one*-dimensional Rouse motion along the tube into three dimensions (see Eq. 6.37 in Ref.<sup>4</sup>)

$$\langle \delta \mathbf{R}^2(t) \rangle = \langle a_{pp} |\delta s(t)| \rangle = a_{pp} \sqrt{\frac{2}{\pi} \langle \delta s(t)^2 \rangle} , \quad (35)$$

where the first equal sign follows since the primitive-path adopts a random walk conformation with step-length  $a_{pp}$  and  $\delta s(t)$  denotes the curvilinear displacement of a bead along the

primitive-path curve. The second equal sign follows from the relation between the mean magnitude and the root-mean-square moment for a Gaussian distributed random variable. Using  $\langle \delta s^2 \rangle = g_1(t)/3$  with Eqs. (31) and (30) and applying continuity between the different power-law regimes, Hou<sup>67</sup> determined the prefactors Doi and Edwards<sup>4</sup> had neglected in assembling the various scaling laws and crossovers:

$$g_1(t) = \frac{2}{\pi^{3/2}} l_K^2 \times \begin{cases} \frac{t}{\tau_K} & t \ll \tau_K \\ \left(\frac{t}{\tau_K}\right)^{1/2} & \tau_K \ll t \ll \frac{\pi}{9} \tau_e \\ N_{eK} \left(\frac{\pi}{9}\right)^{1/4} \left(\frac{t}{\tau_e}\right)^{1/4} & \frac{\pi}{9} \tau_e \ll t \ll \pi \tau_R \\ N_K \left(\frac{t}{\tau_{max}}\right)^{1/2} & \pi \tau_R \ll t \ll \pi \tau_{max} \\ \frac{1}{\sqrt{\pi}} N_K \frac{t}{\tau_{max}} & \pi \tau_{max} \ll t \end{cases} . \quad (36)$$

In particular, he demonstrated that accounting for these numerical constants is essential for quantitative estimates of the entanglement time<sup>68-71</sup> and quantitative comparisons between PPA based predictions of the tube model and dynamical measurements. Finally, we obtain for  $g_3(t)$

$$g_3(t) = \frac{2}{\pi^{3/2}} l_K^2 \times \begin{cases} \frac{N_{eK}^2}{\sqrt{\pi} N_K} \left(\frac{t}{\tau_e}\right) & t \ll \frac{\pi}{9} \tau_e \\ \frac{N_{eK}}{3} \left(\frac{t}{\tau_R}\right)^{1/2} & \frac{\pi}{9} \tau_e \ll t \ll \pi \tau_R \\ \frac{N_{eK}}{3\sqrt{\pi}} \frac{t}{\tau_R} & \pi \tau_R \ll t \end{cases} . \quad (37)$$

### 3 Methods

The present, more technical section describes the methods we have employed. Besides providing details on our Molecular Dynamics simulations (Sec. 3.1) and the way we set up the systems (Sec. 3.2), we define the estimators we use to extract the Kuhn length (Sec. 3.3), describe the primitive path analysis used to estimate the entanglement length (Sec. 3.4), and our strategy for extracting the effective bead friction in KG melts (Sec. 3.5).

### 3.1 Molecular Dynamics Simulations of the Kremer Grest Model

We have carried out two types of KG simulations. For our fully interacting reference melts, we use the standard KG<sup>19</sup> choice of  $\Gamma = 0.5m_b\tau^{-1}$  for the friction of the Langevin thermostat. As a complement, we have also simulated non-interacting “phantom” bead-spring polymers (Sec. 2.4) with a suitably renormalized bending stiffness,  $\tilde{\kappa}(\kappa)$ , using the same approach. In this case, we employ the effective bead friction in the fully interacting systems,  $\Gamma = \zeta_b$ . Note that Eq. (4) reduces to the overdamped limit, Eq. (11), for  $t > m_b/\zeta_b$ . For a time step of  $\Delta t$ , the noise amplitude is given by  $\langle \boldsymbol{\xi}_i(t) \cdot \boldsymbol{\xi}_j(t') \rangle = \frac{6\Gamma k_B T}{\Delta t} \delta_{i,t'} \delta_{ij}$ .

For integrating the Langevin dynamics of our systems, we use the Grønbech-Jensen/Farago (GJF) integration algorithm<sup>72,73</sup> as implemented in the Large Atomic Molecular Massively Parallel Simulator (LAMMPS).<sup>74</sup> This integrator has the feature that the conformational temperature is exact, while the kinetic temperature is correct to  $O(\Delta t^2)$  accuracy. In practice, this means that positions are exactly Boltzmann distributed as expected from the force field and the preset temperature of the thermostat, while the velocity distribution is only approximately the Maxwell-Boltzmann distribution expected at the preset temperature. The systematic error in velocities are of the order of  $O(\Delta t^2)$ . Most thermostats add or subtract heat in response to the instantaneous kinetic temperature, since this observable is trivial to obtain and use in a feed-back control loop. As a result, such a thermostat will instead make an unknown time step dependent integration error in the conformational temperature.<sup>72</sup> The effects of such an error is quite difficult to detect and correct for, whereas an error in the kinetic temperature is easy to detect, and can be fixed trivially by decreasing the time step. In practice, this error also reflected in dynamic properties for instance the diffusion coefficient estimated from mean-square displacements (of positions) or from the integrated autocorrelation function (of velocities) would incur a time step size dependent systematic Langevin integrator error depending on the design of the integrator. With our choice of  $\Delta t = 0.01\tau$  time step, the average kinetic temperature is  $T = 0.979\epsilon$  for KG melt states indicating a Langevin integrator error of the order of 2%.



To accurately estimate the time dependent shear relaxation modulus we follow the approach of Ramirez et al.<sup>75</sup> We use the correlator algorithm that they implemented in LAMMPS and include both the autocorrelation of the off-diagonal elements of the stress tensor as well as the autocorrelation of the normal stresses. In simulations where we aim to study static properties we aim for a single system system of sizes of  $\sim 5 \times 10^6$  beads. However, for sampling dynamic properties, we instead run five statistical independent samples of systems of typical size  $5 - 10 \times 10^4$  beads.

## 3.2 System setup and equilibration

We have generated equilibrated entangled KG model melt states both for unentangled or weakly entangled systems as well as for moderately to highly entangled melts. We used brute force equilibration methods for the weakly entangled systems, while we set up the moderately and highly entangled melts using a sophisticated multiscale process, which we developed recently.<sup>76</sup>

### 3.2.1 Brute-force equilibration of weakly entangled systems

In the case of weakly entangled melts, the oligomers were randomly inserted in the simulation domain, and the energy was minimized using the force-capped interaction potential and subsequently transferred to the KG force-field as in Ref.<sup>76</sup> The resulting conformations were then simulated using Molecular Dynamics as above, while also performing double bridging Monte Carlo moves<sup>77,78</sup> as implemented in LAMMPS.<sup>79</sup> During these moves, bonds are swapped between different chains in such a way that the melt remains monodisperse. Such connectivity altering moves are known to accelerate the equilibration by side stepping potential barriers to the physical dynamics.

To characterize the Kuhn length dependence of stiffness, we performed brute force simulations of weakly entangled melts with nominal chain length  $N_K = 10, 20, 40, 80$  for varying chain stiffness using the approximate Kuhn length estimate from Ref.<sup>76</sup> During the produc-

tion run, we continued to perform double bridging moves. To estimate the Kuhn friction dependence of stiffness, we equilibrated oligomer melts with nominal length  $N_K = 1, 3, \dots, 30$  and varying stiffness as above. Our production runs were up to  $2 - 10 \times 10^5 \tau$  steps long and performed without the double bridging moves. The computational effort was about 60 core years of simulation time.

A good measure for the length of the simulation where double bridging takes place is the number of displacement times. A displacement time is the time it takes the mean-square bead displacement to match the chain mean square end-to-end distance. This measure is well defined in our case where we apply connectivity altering Monte Carlo<sup>77-79</sup> moves during the simulations, whereas the chain center of mass can not be defined in this case. During the analysis, the data obtained within the first displacement time was discarded, and trajectory data for subsequent displacement times were binned and averaged assuming statistical independent results for each displacement time bin. We report mean-square internal distances sampled over at least five displacement times for the longest and stiffest chains and well in excess of 1000 displacement times for shorter and less stiff chains.

### 3.2.2 Multi-scale equilibration of highly entangled systems

For estimating the number of Kuhn segments between entanglements and the Kuhn time, we required highly entangled melts. To prepare such states, used an effective multiscale equilibration process<sup>76</sup> which transfers melt states between three computationally different, but physically equivalent polymer models. We initially equilibrate a lattice melt where density fluctuations are removed using Monte Carlo simulated annealing. We choose the tube diameter as the lattice parameter, such that approximately 19 entanglement segments occupy the same lattice site. The lattice melt state is then transferred to an auxiliary KG model, where WCA pair-forces are capped. The pair-forces are chosen such that local density fluctuations are further reduced compared to the lattice melts, while also partially allowing chains to move through each other. This auxiliary model produce Rouse dynamics, and we

simulate the dynamics for sufficiently long to equilibrate the random walk chain structure beyond the lattice length scale. Finally we transfer the auxiliary model melt state to the KG force field, and equilibrate local bead packing. The three models were designed to reproduce identical large scale chain statistics, and the two MD models were designed to produce the same local chain statistics, which required using a renormalized bending stiffness in the auxiliary model. The first set of data we prepared using this approach comprises systems with fixed numbers of beads  $N_b = 10000$  and varying chain stiffness. The effective chain length, measured in numbers of entanglements per chain, varies between  $Z(\kappa = -1) = 85$  to  $Z(\kappa = 2.5) = 570$ . To check for finite length effects for the flexible melts with  $-1 < \kappa < 0$ , we generated additional melts with fixed number of entanglements  $Z = 200$  and varying number of beads. The total computational effort of preparing these entangled melts was about 12 core years. As a quality check, we monitor (i) density fluctuations and (ii) the single chain statistics.<sup>57</sup> The melt structure factor,  $S(q)$ , is constant on all scales above the bead size, documenting the absence of all long-wave length density fluctuations as expected from a nearly incompressible system (data not shown). Fig. 1 shows excellent agreement between the reduced mean-square internal distance,  $\langle(\mathbf{R}_i - \mathbf{R}_{i+n})^2\rangle/n$  for brute force equilibrated melts of chains of medium length and for the highly entangled melts with  $Z \geq 200$ , which we have prepared by our multiscale equilibration process.

### 3.3 Estimating the Kuhn length

The incompressibility of polymer melts induces weak long range repulsive interaction along the chain, which manifest themselves in long-range bond orientation correlations.<sup>44,45,58-60</sup> If  $\langle R^2(l) \rangle_L$  denotes the mean-square spatial distance of beads separated by a contour distance  $l$  along a chains in a monodisperse melt of chains of length  $L \geq l$ , then  $\langle R^2(l) \rangle_L < \lim_{L \rightarrow \infty} \langle R^2(l) \rangle_L$ . With local estimators risking to underestimate the true Kuhn length, we

propose to use a global estimator based on eq. (10),

$$l_K = \lim_{l \rightarrow \infty} \lim_{L \rightarrow \infty} l_K(L^{-1/2}, l^{-1/2}) \quad (38)$$

$$l_K(L^{-1/2}, l^{-1/2}) = \frac{\langle R^2(l) \rangle_L}{l}, \quad (39)$$

and to fit data for finite internal distances,  $l$ , on chains of finite length,  $L$ , to a polynomial of the form

$$l_K(L^{-\frac{1}{2}}, l^{-\frac{1}{2}}) = l_K + c_{10}L^{-\frac{1}{2}} + c_{01}l^{-\frac{1}{2}} + c_{20}L^{-1} + c_{11}L^{-\frac{1}{2}}l^{-\frac{1}{2}} + c_{02}l^{-1} \quad (40)$$

motivated by the theory of Wittmer et al.<sup>58</sup>

### 3.4 PPA for estimating entanglement lengths

The entanglement length can be estimated via a primitive path analysis<sup>80</sup> of the microscopic topological state of entangled melts. The idea<sup>81,82</sup> is to fix the chain ends and to convert the chains into rubber bands, which contract without being able to cross. This is achieved by minimizing the potential energy for fixed chain ends and disabled intrachain excluded volume interactions. We performed the minimization by using the steepest descent algorithm implemented in LAMMPS. The minimization is followed by damped Langevin dynamics as in the standard PPA algorithm. We performed a PPA that preserves self-entanglements by only disabling interactions between pairs of beads within a chemical distance of  $2N_{eK}$  Kuhn segments along the chain. The computational effort for the PPA analysis is insignificant in comparison to the other observables.

Primitive paths are locally smooth, kinked at entanglement points between different chains, and have the same large scale random walk statistics as the original chains<sup>4,83</sup> (see Fig. 3). In particular, primitive paths can be characterized by a contour length,  $L_{pp} < L$ , and a Kuhn length,  $a_{pp} > l_K$ . From the relation  $l_K L = \langle R^2 \rangle = a_{pp} L_{pp}$ , it follows that

$a_{pp}/l_K = L/L_{pp}$ , i.e. during PPA the Kuhn length increases in inverse proportion to the shortening of the contour length. Assuming random walk statistics between entanglement points,  $a_{pp}^2 = l_K^2 N_{eK}$ , one obtains the classical estimator<sup>4,80,83</sup>

$$N_{eK}^{classical} = \frac{a_{pp}^2}{l_K^2} = \frac{L^2}{L_{pp}^2}, \quad (41)$$

of the number of Kuhn segments per entanglement length as function of a convenient PPA observable, the ratio of the contour length of the primitive paths and of the original chains.

$N_{eK}^{classical}$  suffers from finite  $Z$  effects, when applied to the relatively short chain melts, that can be equilibrated by brute-force molecular dynamics. Hoy et al.<sup>84</sup> showed that eq. (41) provides a lower bound on the true entanglement length and suggested another estimator that provides an upper bound

$$N_{eK}^{Hoy} = N_K \left( \frac{L_{pp}^2}{\langle R^2 \rangle} - 1 \right)^{-1}. \quad (42)$$

For flexible chains the Kuhn length of the PPA path,  $a_{pp}$ , and the contour distance,  $l_e$ , between entanglements along the primitive path are proportional to each other.<sup>83</sup> However, as chain stiffness increases, the assumption of random walk statistics between entanglements becomes questionable (see e.g. Fig. 3). To correct for this effect,<sup>46</sup> one can assume WLC statistics in equating  $l_e$  with the root mean-square *spatial* distance between entanglement points

$$l_e^2 = \langle R^2(N_{eK}; l_K) \rangle \approx l_K^2 N_{eK} (1 - [1 - \exp(-2N_{eK})]/[2N_{eK}]) . \quad (43)$$

Since the PPA contour length is given by  $L_{pp} = Zl_e$  and the contour length of the original chain by  $L = l_K N_K = ZN_{eK}l_K$ , this suggests a different relation between  $N_{eK}$  and the square of the contour length contraction ratio,

$$\left( \frac{L_{pp}}{L} \right)^2 = \frac{2N_{eK} + \exp(-2N_{eK}) - 1}{2N_{eK}^2} . \quad (44)$$

Eq. (44) is straightforward to invert numerically for any measured contraction ratio. In the limit of  $N_{eK} \gg 1$ , it reduces to  $N_{eK} = L^2/L_{pp}^2$  consistent with Eq. (41). In the limit,  $N_{eK} \ll 1$ , eq. (44), remains valid and converges to the Semenov expression for entanglement length in tightly entangled semi-flexible chains.<sup>46,85,86</sup>

### 3.5 Estimating the effective bead friction

In the logic of the tube model<sup>4</sup> we are interested in  $\zeta_b = \zeta_{cm}/N_b$  in Eq. (11) for *unentangled* chains. The fact, that the asymptotic diffusion of long chains is slowed down by entanglement effects,<sup>4,64</sup> is in itself not a major obstacle, because according to the tube model we should still be able to use Eq. (12) for chains of arbitrary length as long as we limit the analysis to short enough times compared to the entanglement time. However, the Rouse and tube models discussed in the previous section are so well established,<sup>4</sup> that it is easy to forget how drastic the approximations are, which are underlying the description. In particular, experiments and simulations<sup>19,87-95</sup> show an accelerated early-time CM diffusion, which can be explained<sup>51-54</sup> through correlation-hole effects and viscoelastic hydrodynamic interactions. As a consequence, (i)  $\zeta_{cm}$  has to be extracted from long-term diffusion data and (ii)  $\zeta_b$  has to be inferred via a double extrapolation beyond the monomer scale (to reduce end effects<sup>96</sup>) and below the entanglement scale (to extract the effective friction constant for the local, topologically unrestricted motion).

In contrast to the CM motion, the monomer dynamics is hardly affected by correlation-hole effects and viscoelastic hydrodynamic interactions.<sup>52,54</sup> In particular, the local dynamics is independent of chain length and, on sufficiently small scales, entanglement effects. On the downside, (i) KG chains show ballistic motion at very short times, (ii) they are obviously not flexible below their respective Kuhn lengths, and, most importantly, (iii) the analysis of the chain statistics shows that commodity polymers (and corresponding KG models) are not even fully flexible on the entanglement scale.<sup>43</sup> As a consequence, it is desirable to separately deal with the two *independent* approximations underlying the standard Rouse and

tube models for flexible polymer dynamics: the Gaussian chain model and the assumption, that the (local) dynamics can be described by a single-chain Langevin equation, Eq. (11).

Langevin simulations of phantom KG chains (Sec. 2.4) account for bead inertia and effective local chain stiffness. The only input required are estimates of the Kuhn length,  $l_K$ , and of the bead friction,  $\zeta_b$ , in the fully interacting systems. To validate the single-chain description *independently* of chain stiffness, it suffices to compare the dynamics of the fully interacting and the phantom systems at times up to the entanglement time.

## 4 Results

Below we present our simulation results for the chain structure and dynamics in KG melts. We start out from the conformational statistics (Sec. 4.1) to extract the Kuhn length as a function of the bending rigidity (Sec. 4.2). Next we turn to the primitive path analysis of the microscopic topological state and the entanglement length (Sec. 4.3). To estimate the bead friction in KG melts, we analyse the center-of-mass motion (Sec. 4.4). In a second step, we analyse the monomer diffusion and validate our choice of the bead friction through a comparison to the dynamics of Phantom KG chains (Sec. 4.5).

### 4.1 Conformational statistics

The mean-square internal distances,  $\langle(\mathbf{R}_i - \mathbf{R}_j)^2\rangle$ , between beads  $i, j$  as a function of their contour distance,  $L_{ij} = l_b|i - j|$ , provide a convenient overview of the chain statistics on different length scales. The small filled symbols in the inset of Fig. 1 show the reduced internal distances,  $\langle(\mathbf{R}_i - \mathbf{R}_j)^2\rangle/L_{ij}$ , for our brute force equilibrated KG melts of chains of medium length. The data exhibit a monotonous increase to a plateau, which is reached at chemical distances much larger than the Kuhn length. A priori, the plateau height matches the Kuhn length of the chains, Eq. (9). However, when analyzing the data, care must be taken to account for slowly decaying power law corrections (see below).

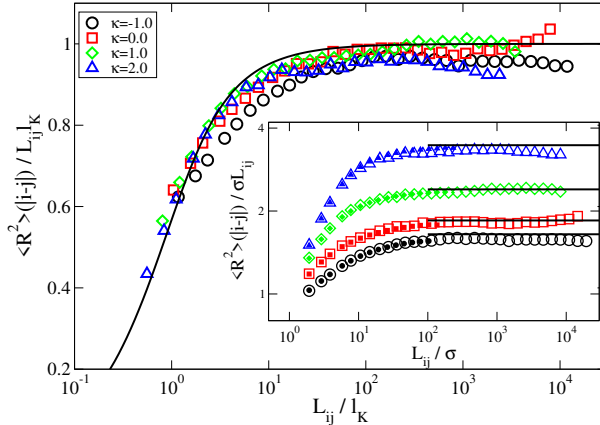


Figure 1: Reduced mean-square internal distances as a function of contour distance for different values of the effective bending stiffness ( $(\kappa = -1)$ /black,  $(\kappa = 0)$ /red,  $(\kappa = 1)$ /green, and  $(\kappa = 2)$ /blue). Main figure: Kuhn units, inset: LJ units. Small filled symbols represent data for brute force equilibrated, moderately entangled melts with  $N_K = 80$ . Large open symbols show data for highly entangled melts with  $Z \geq 200$ , which we generated by an efficient multi-scale equilibration procedure<sup>76</sup>. In the inset we show our estimates of the Kuhn lengths as black lines. The black line in the main figure represents the wormlike chain expression, Eq. (9).

A typical signature of insufficient equilibration is the appearance of swelling at intermediate length scales, which would be seen as a bump in the figure.<sup>57</sup> Figure 1 also contains results for highly entangled melts with  $Z \geq 200$ , which we have prepared by our multiscale equilibration process.<sup>76</sup> Their excellent agreement with the reference data suggest that these systems are properly equilibrated on all length scales. In addition to validating the single-chain statistics, we have also sampled the the structure factor for these melts (see Ref. ,<sup>76</sup> data not shown for the present systems). The structure factor is constant on all scales above the bead size. As expected for a nearly incompressible system, there are no long-wave length density fluctuations.

## 4.2 Kuhn length

We have estimated the asymptotic value of the Kuhn length, Eq. (38), for all studied values of chain stiffness  $\kappa$ , on the basis of our “gold standard” reference data for brute-force equilibrated melts. To do so, we fitted mean-square internal distances,  $\langle R^2(l) \rangle_L$ , by the



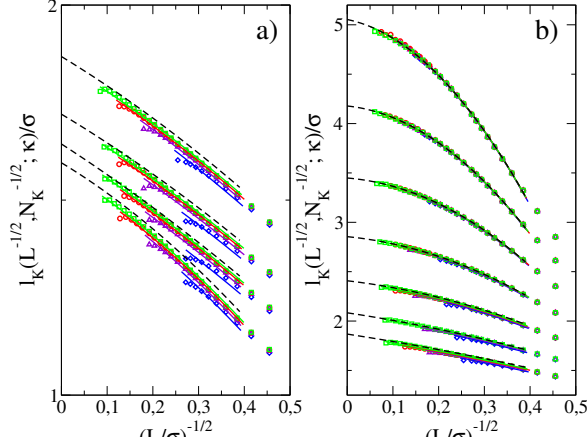


Figure 2: Kuhn length extrapolation for melts of nominal chain length  $N_K = 10, 20, 40, 80$  (denoted by blue diamond, orange triangle up, red circle, and green box, respectively) for flexible melts with  $\kappa = -2, -1, -0.5, 0$  (bottom to top in panel a), and semi-flexible melts with  $\kappa = 0, 0.5, 1.0, 1.5, 2.0, 2.5, 3.0$  (bottom to top in panel b). Shown are also the results of the fits of eq. (40) to individual melts (solid lines matching the melt colors) and the extrapolation to infinite chain length as function of contour length (black dashed line).

ansatz Eq. (40). The  $c_{nm}$  parameters account for the sub-dominant finite size effects in our data. During the fitting,  $c_{01}$  and  $c_{11}$  terms are restricted to be negative or zero. This ensures that the limit of infinite contour length is approached from below. Fits were performed on data with  $l > 6.25\sigma$ . This was chosen to ensure some data points from the shortest melts still contribute to the analysis, while discarding data necessitating the inclusion of further subdominant terms in our ansatz Eq. (40).

Fig. 2 shows data for the finite size estimates of the Kuhn length along with the results of our extrapolation scheme for flexible and semi-flexible KG systems (panel a and b, respectively). As the contour length is increased the Kuhn length estimate increases monotonously towards the limit given by the intercept with the y axis. For the semi-flexible systems (panel b), we observe a good collapse of the data from melts with different chain length, whereas for the flexible systems the data collapse is less good indicating that finite size effects are more important in the limit of flexible chains. For the flexible melts, we also see a systematic downturn for the data points corresponding to the longest contour lengths, which demonstrates that care should be taken in choosing the range of data used for the extrapolation.

Also shown in the figure are predictions of finite size Kuhn lengths from the fits and the limit of infinite chain length. We see good agreement of the fits to our data. The extrapolation to infinite melt chain length is in very good agreement with all data for the semi-flexible melts, but we observe that it is systematically above the data for the flexible melts. This illustrates the importance estimating the asymptotic Kuhn length using data from melts with several chain lengths simultaneously. For instance, extrapolating the  $N_K = 80$  data towards infinite contour length i.e. extending the solid green lines to the intercept with the axis would underestimate the true limiting Kuhn length value for all the flexible melts.

### 4.3 PPA and Entanglement length

Figure 4 shows our results for the dependence of the number of Kuhn segments between entanglements on chain stiffness. As chains become stiffer, their spatial size increases, and hence the chains become more strongly entangled as already expected from Fig. 3. This leads to the observed progressive decrease in the number of Kuhn units between entanglements. Note that if we continue to increase the stiffness far above  $l_K \gg 10\sigma$  i.e.  $\kappa \gg 6$ , then we expect the onset of a isotropic to nematic transition.<sup>38</sup>

We observe excellent agreement between the classical estimator eq. (41) and the Hoy estimator eq. (42) indicating that our melts are sufficiently long for finite-size effects to be irrelevant. We also observe good agreement between our new estimator eq. (44) and the other estimators for flexible chains with  $N_{eK} > 10$ , but for the stiffer and more entangled chains, we can see that the previous estimators progressively overestimate the number of entanglements by up to 20% for the melts with the stiffest chains. The solid line shown in Figure 4 is an empirical interpolation given by eq. (56) to describe the dependence of the entanglement length on stiffness.

A potential source of error is the neglect of self- and image-entanglements in the simplest PPA algorithm,<sup>80</sup> which disables all intra-chain excluded volume interactions. The results reported here were obtained with a local version of PPA<sup>99</sup> which preserves self- and

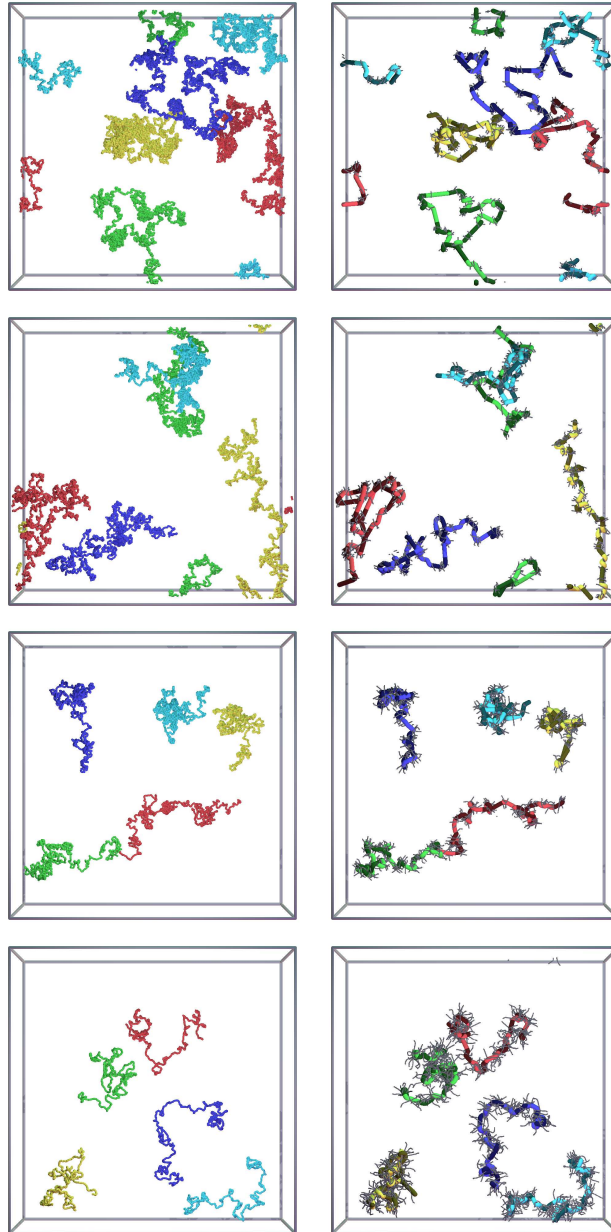


Figure 3: Visualization of the same five chains in the melt state (left) and their primitive-path (right) for stiffness  $\kappa = -1, 0, 1, 2$  (top to bottom), respectively, for melts with constant number of entanglements  $Z = 20$ . The entanglement length is illustrated as an alternating color saturation along the primitive-paths. Short segments of the entanglement partners are also shown along the primitive-paths (thin gray lines).

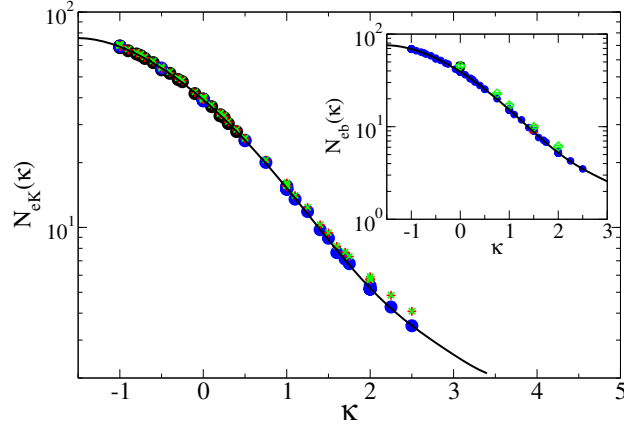


Figure 4: Number of Kuhn segments between entanglements  $N_{eK}$  vs stiffness parameter for the KG polymer melts. Our finite  $N_{eK}$  corrected estimate eq. (44)  $85 < Z < 200$  (black  $\circ$ ), and  $Z > 200$  (blue  $\circ$ ), the classical estimator eq. (41) (red  $+$ ), the Hoy estimator eq. (42) (green  $\times$ ). The inset shows a comparison of our estimated  $N_{eK}$  (small blue circles) compared to literature results from Hoy et al.<sup>97</sup> (black circle), Hsu et al.<sup>71</sup> (red box), and Moreira et al.<sup>98</sup> (green diamonds). Our interpolation eq. (56) is also shown (solid black lines).

image-entanglements. While we had shown previously that self-entanglements may be safely neglected,<sup>99</sup> we briefly address the issue of image-entanglements. The problem is easily understood for the extreme case of a melt composed of a single chain in periodic boundary conditions, which would appear to be unentangled in the simple version of the algorithm. In general, the importance of image-entanglements depends on the ratio  $r = V^{1/3}/(l_K(\kappa)\sqrt{N_K})$  where  $V$  is the volume of the cubic simulation box. Ideally, systems should be much larger than the individual chains i.e.  $r > 1$  to limit self-interactions. However for very long chains, it is difficult to fulfil this condition. For the our melts with  $N_b = 10000$  the ratio varies from  $r(\kappa = -1) = 1.8$  down to  $r(\kappa = 2) = 1.3$  suggesting that we should not expect significant finite box size effects.<sup>98</sup> Nonetheless, when we submitted our PPA meshes to a subsequent PPA analysis disregarding all self- (and hence also image) entanglements, we found indeed only a small but systematic increase of the entanglement length by 3.5%, which we observed to be independent of chain stiffness.

Figure 4 also contains previous PPA results from the literature. Hoy et al.<sup>97</sup> estimated the asymptotic entanglement length for  $\kappa = 0$  using melts of  $N_b = 100, \dots, 3500$  for constant

total numbers of beads. In this case, while their longest chains reach  $Z(\kappa = 0) = 46$ , the sample contained only as few as  $M = 80$  chains. These melts were equilibrated using double bridging. Hoy et al. obtained  $N_{eb} = 86.1$ . Hou et al. estimated the systematic error due to various PPA algorithms and the extrapolation schemes to be  $\pm 7$ .<sup>17</sup> Recently, Moreira et al.<sup>98</sup> used more powerful equilibration methods and were able to equilibrate melts up to  $N_b = 2000$  and  $M = 1000$  for stiffness  $\kappa = 0, 0.75, 1, 1.5, 2$  i.e.  $Z(\kappa = 0) = 26$  up to  $Z(\kappa = 2) = 97$  entanglements. Finally, Hsu et al.<sup>71</sup> equilibrated melts up to  $N_b = 2000$  for  $\kappa = 1.5$  (i.e.  $Z = 74$ ). These results appears to be in good agreement with our data. We see that Literature data are slightly but systematically above our data, which could be explained by the usage of a Kuhn length that has not been corrected for incompressibility effects and/or the use of the old PPA estimators which do not correct for stiffness.

#### 4.4 Center-of-mass motion

Figure 5 shows our results for the CM motion of KG and phantom KG chains. The different panels display  $g_3(t)$  for varying chain lengths for four characteristic values of the reduced bending stiffness,  $\kappa$ . Data for fully interacting KG melts are shown as symbols, while results for corresponding Phantom KG chains are represented as solid lines. In Figure 5 we plot  $g_3(t)N_b/t$ , because in this representation data should collapse to a horizontal line,  $6k_B T/\zeta_b$ , if the chains CM exhibited simple diffusion with a chain length independent friction per bead,  $\zeta_{cm} = N_b\zeta_b$ , as assumed by the Rouse model. By construction this is the behavior shown by the Phantom KG model (Eq. (13)) after an initial ballistic regime. The objective of the present and the subsequent section is to justify and validate our choice of the effective bead friction,  $\zeta_b$ , in single-chain models for KG melts.

In agreement with previous computational<sup>19,40,71,100</sup> and theoretical results,<sup>4,44,52</sup> fully interacting chains in KG melts show a more complex behavior than Phantom KG chains. At the earliest times, the chains move ballistically in perfect agreement with their phantom counterparts. At intermediate times, the CM motion is accelerated relative to the phantom

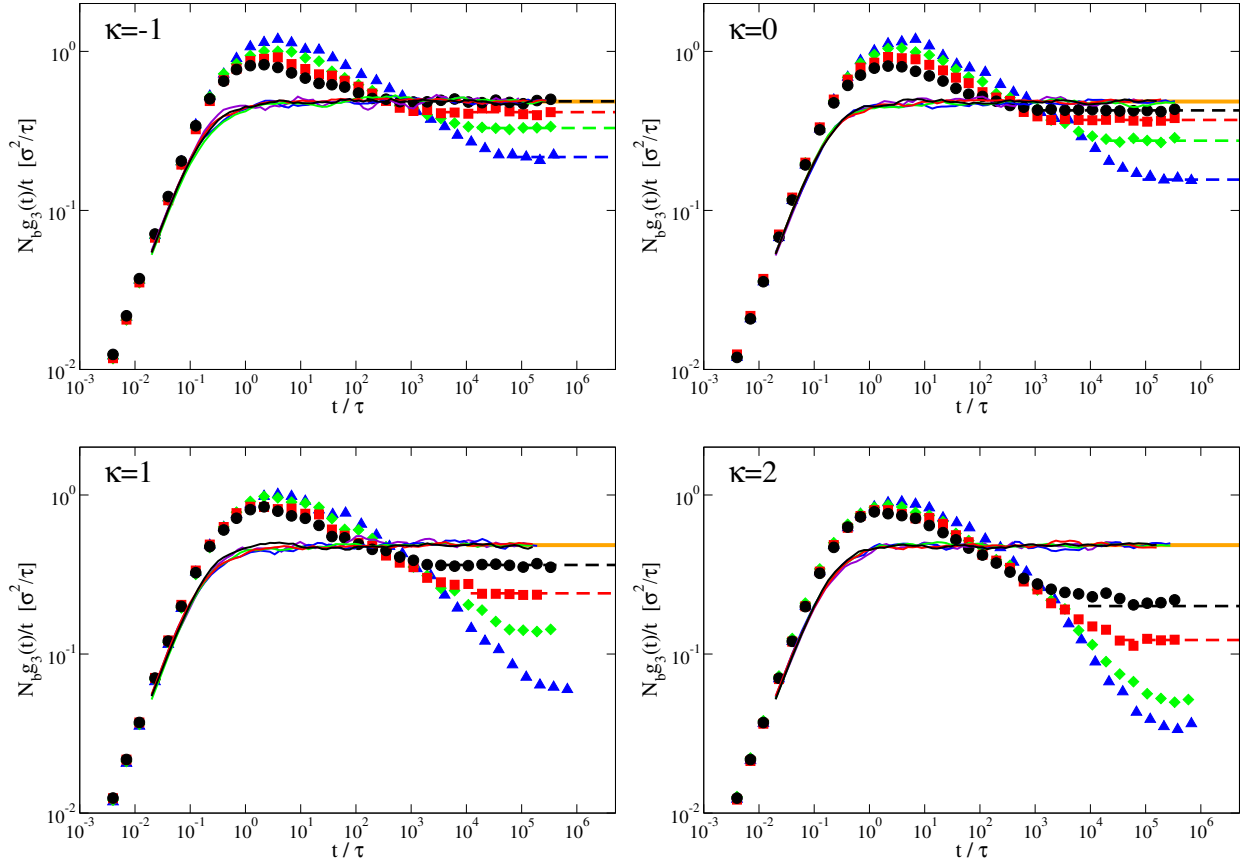


Figure 5: Normalized CM mean-square displacements,  $g_3(t)N_b/t$  as a function of time. Colors indicate chain length ( $N_K = 10, 20, 40, 80, 160$  shown as black, red, green, blue, violet, respectively), panels show results for different values of chain stiffness. Symbols represent data for KG melts, solid lines results for corresponding phantom KG chains. Dashed lines indicate our fits of the long-time diffusion, Eq. (12), in the fully interacting system. The theoretical phantom prediction  $g_3(t)N_b/t = 6k_B T / \zeta_b$  is shown as thick orange line.

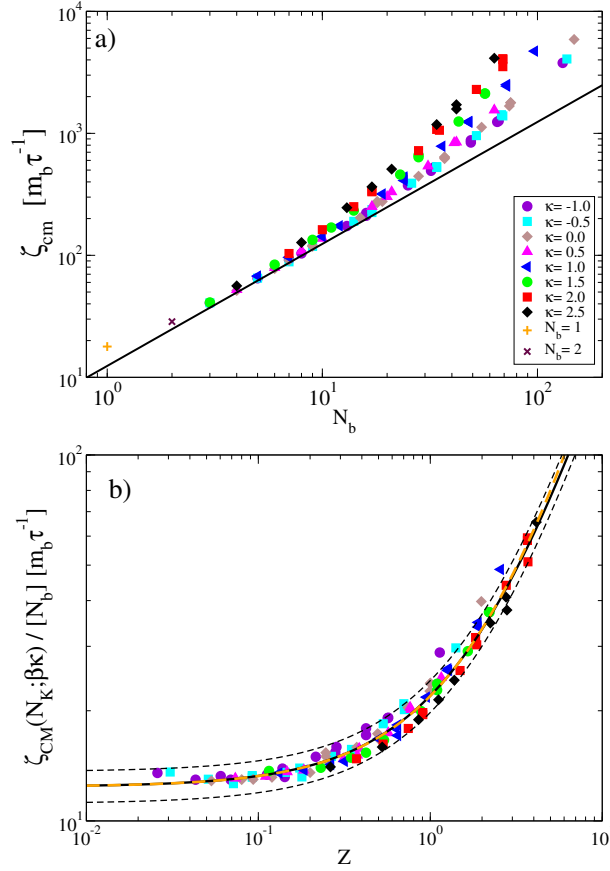


Figure 6: Measured CM friction as function of chain length (a) and estimated bead friction as function of number of entanglements (b). Colors indicate chain stiffness. Shown is also the Rouse approximation  $\zeta_{cm}(N_b) = \zeta_b N_b$  (a: solid black line), the polynomial approximant eq. (46) (b: orange dashed line), and the empirical Padé approximant eq. (47) (b: solid line, dashed line indicate a 10% error of  $\zeta_b$ ).

chains and relative to their own asymptotic diffusion. In agreement with previous computational and theoretical results,<sup>51–54</sup> the effect is stronger for longer chains. In the asymptotic regime the order is reversed with a stronger spreading for stiffer, more strongly entangled chains.

In the following, we focus on the long-time diffusion of unentangled and weakly entangled chains with  $N_K = 1, 2, 3, 4, 5, 8, 10, 15, 20, 30, 40, 80$ . For completeness, we have also simulated KG monomers and dimers,  $N_b = 1, 2$ , whose dynamics is independent of chain stiffness, as well as trimers,  $N_b = 3$ , which are the shortest chains which could exhibit a  $\kappa$ -dependent dynamics. In all cases, we have obtained the CM diffusion constant,  $D_{cm}$ , from Eq. (12) by sampling plateau values of  $g_3(t)/[6t]$  for log-equidistant times and discarding simulations where the standard deviation of the sampled values exceeded 5% of their average value. The fits are indicated by the dashed lines in Fig. 5. Figure 6a shows the increase of the CM friction constant,  $\zeta_{cm}(N_b) = k_B T / D_{cm}(N_b)$ , with chain length. For very short oligomers, the apparent bead friction,  $\zeta_{cm}(N_b)/N_b$ , decreases slightly with increasing chain length:  $\zeta_{cm}(1)/1 = 17.9m_b\tau^{-1}$ ,  $\zeta_{cm}(2)/2 = 14.3m_b\tau^{-1}$ , while  $12.9m_b\tau^{-1} \leq \zeta_{cm}(\kappa)(3)/3 \leq 13.8m_b\tau^{-1}$ . For longer chains, the apparent bead friction increases with chain length. For our stiffest and most strongly entangled systems the effect sets in already at  $N_b = 4$ . For our most flexible systems, the apparent bead friction plateaus at  $\zeta_{cm}(N_b)/N_b = 12.4m_b\tau^{-1}$  around  $N_b = 10$ .

Figure 6b shows our results for the apparent bead friction for all chains with  $N_b \geq 3$  as a function of chain length in entanglement units,  $Z = N_b/N_e(\kappa)$ . They allow us to draw non-trivial conclusions from three independent observations:

1. Contrary to experiment,<sup>96</sup>  $\zeta_{cm}(N_b)/N_b$  essentially reaches a plateau for short chain KG melts. Plausibly, studying the model with purely repulsive interactions at constant density,  $\rho_b = 0.85\sigma^{-3}$ , avoids the need for an iso-free-volume correction<sup>96</sup> of the data.
2. The upturn can be safely attributed to entanglement effects, because it occurs for all systems at the same effective chain length,  $Z = N_b/N_e(\kappa)$ . With  $N_e(\kappa)$  being independently derived from PPA, this is additional strong evidence that the results of



this *static* analysis of the microscopic topological state is relevant to the chain *dynamics*.

3. The collapse of the data for different values of  $\kappa$  suggests a *stiffness independent* value of

$$\zeta_b = 12.4m_b\tau^{-1} \quad (45)$$

for the microscopic bead friction, which we use in theoretical calculations throughout the remainder of the data analysis as well as in the simulations of the Phantom KG chains. The scatter of the data for weakly entangled systems suggests an error bar on the bead friction estimate below 10%. For comparison, Kremer and Grest<sup>19</sup> obtained  $\zeta_b = 16 \pm 2m_b\tau^{-1}$  for the standard KG model with  $\kappa = 0$  from the CM motion of chains with  $Z \approx 1$  and a Rouse mode analysis of their internal dynamics. Note, however, that at this point it is difficult to ascertain this value with high precision for stiffer chains, since entanglement effects affect their CM diffusion already for very short chains.

So far, we have only made use of the fact that the data perfectly collapse, when plotted as a function of  $Z$ , to conclude, that the effective bead friction is independent of stiffness, Eq. (45). Also included in Figure 6 is the result of a fit of the function

$$f(Z) \equiv \frac{\zeta_{cm}(Z)}{N_b\zeta_b} = \frac{D_{cm}^{(Rouse)}(Z)}{D_{cm}(Z)} = \frac{\tau_{max}(Z)}{\tau_{max}^{(Rouse)}(Z)} \quad (46)$$

to a second order polynomial,  $f(Z) = 1 + aZ + bZ^2$  with  $a = 0.69$  and  $b = 0.08$ . Asymptotically, we expect  $\lim_{Z \rightarrow \infty} f(Z) = 3Z$  (Eq. (34)), suggesting a Padé-type interpolation between the two limits,

$$f(Z) = \frac{1 + cZ + 3dZ^2}{1 + dZ}, \quad (47)$$

where  $c = a - b/(a - 3) = 0.73$  and  $d = -b/(a - 3) = 0.035$ . This interpolation is shown as the black solid line in Fig. 6 which is both in very good agreement with the simulation data as well as the polynomial within the range of entanglement lengths studied here.

## 4.5 Monomer motion

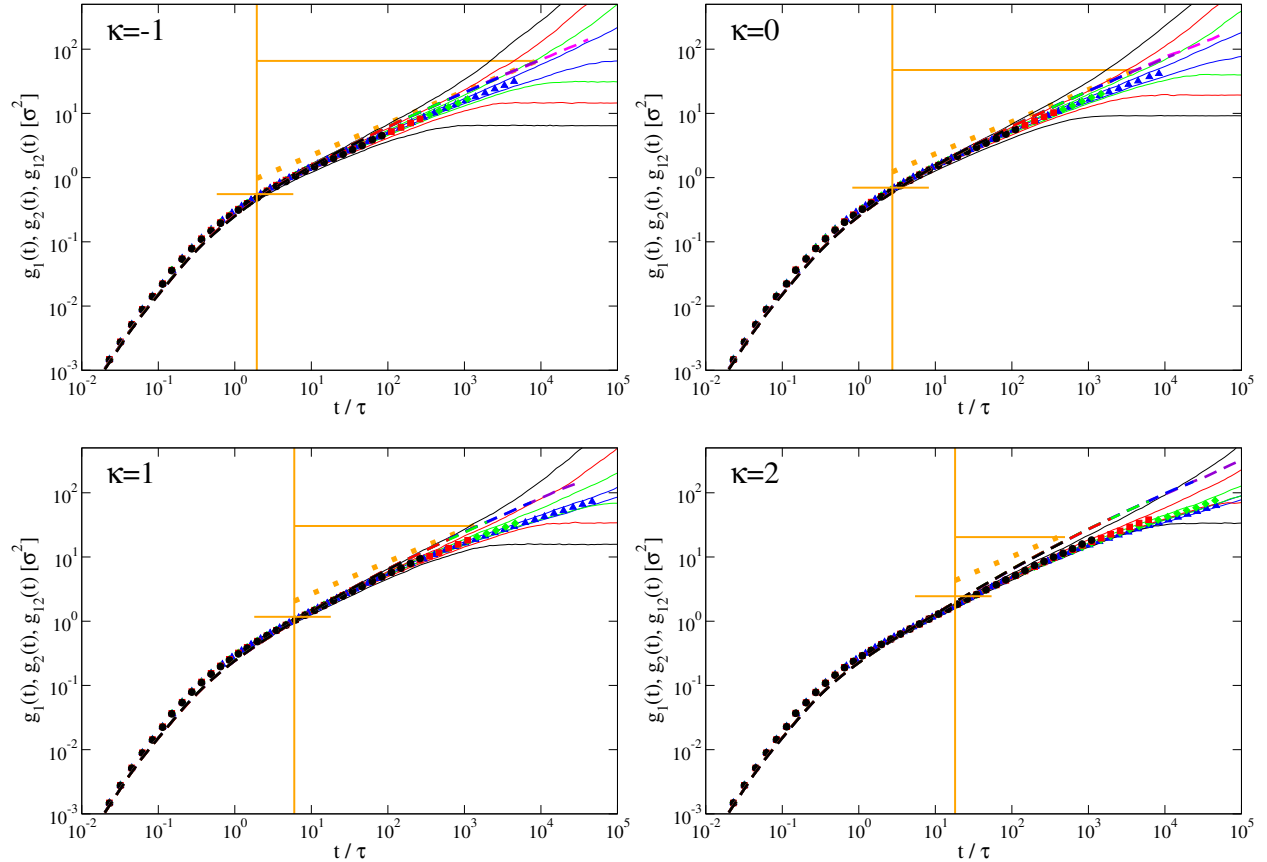


Figure 7: Monomer mean-square displacements  $g_1(t)$ ,  $g_2(t)$  (thin lines) and  $g_{12}(t)$  eq. (48) (symbols) as a function of time for the same systems as in Fig. 5. Also shown are  $g_{12}(t)$  for Phantom KG chains of varying length (dashed lines) and the theoretical prediction of Rouse theory (orange dotted line). Colors indicate chain length, different panels show results for different values of chain stiffness. Also indicated are  $\tau_K$  (vertical orange solid line), the displacements  $2l_K^2 \langle R^2(N_K) \rangle / \pi^{1.5}$  corresponding to a Kuhn segment  $N_K = 1$  and also an entanglement segment  $N_K = N_{eK}$  (horizontal orange solid lines).

Figure 7 shows the monomer motion for the same systems as in Fig. 5. The observation of characteristic features of Rouse dynamics like the sub-diffusive monomer motion, Eq. (17), is limited to a time interval  $\tau_K \ll t \ll \min(\tau_R, \tau_e)$ . For unentangled chains,  $g_2(t)$  levels off on approaching the Rouse time,  $\tau_R$ , while  $g_1(t) = g_2(t) + g_3(t)$  starts to be dominated by the CM diffusion. Interestingly, the two deviations almost cancel, if one considers the geometric

mean,

$$g_{12}(t) \equiv \sqrt{g_1(t)g_2(t)} , \quad (48)$$

of the two standard measures of monomer diffusion. Below the Rouse time,  $g_1(t) \approx g_2(t)$ , so that  $g_{12}(t) \propto \sqrt{t/\tau_K}$ . Beyond the Rouse time,  $\sqrt{g_1(t)g_2(t)} \approx \sqrt{R_g^2 g_3(t)} \propto \sqrt{t/\tau_K}$  has the same scaling for entirely different reasons. Compared to the corresponding results for  $g_1(t)$  and  $g_2(t)$  (shown as thin lines in corresponding colors), results for  $\sqrt{g_1(t)g_2(t)}$  are significantly easier to interpret. Note that we have restricted the latter to times, when  $\sqrt{g_1(t)g_2(t)} \leq R_g^2$  and where the monomer motion is dominated by the internal dynamics. In this way we can be sure to obtain information, which is independent of the results for  $g_3(t)$  for  $t > \tau_R$ , which we have analysed in the previous section.

Like the CM motion, the monomer motion is ballistic at the earliest times. In this regime equipartition assures the perfect agreement between KG chains and their Phantom counterparts. The fact that this agreement extends into the diffusive regime is non-trivial. Firstly, the perfect collapse of melt data for different chain lengths provides further evidence for a chain length independent effective bead friction. Secondly, the excellent agreement with the Phantom KG simulations for *all* values of  $\kappa$  validates our choice, Eq. (45) of a stiffness-independent effective bead friction in the single-chain Langevin equations, Eqs. (11) and (13). In particular, this validation does not require the chains to reach the asymptotic Rouse regime, before entanglements effects modify their dynamics. We note that the melt  $g_{12}(t)$  starts to significantly lag behind the Phantom KG reference curve before the monomers reach the entanglement scale,  $g_1(t) \sim g_2(t) \sim \sqrt{g_1(t)g_2(t)} \ll d_T^2$ . In particular, this deviation occurs before the Phantom KG chains have reached the asymptotic Rouse regime, Eq. (19), which we have indicated in the relevant time interval,  $\tau_K \leq t \leq \tau_e \approx N_{eK}^2 \tau_K$ .

## 5 Discussion

The following discussion of the behavior of KG melts is again organised across increasing length and time scales. We start at the Kuhn scale with an empirical relation between the Kuhn length and the bending rigidity,  $\kappa$ , of our chains and an attempt to rationalize the observed dependence (Sec. 5.1). In a second step, we use the information on the bead friction to define the Kuhn units of friction, time and the viscosity at the bead scale (Sec. 5.2). As a first test of the usefulness of these units, we consider the monomer motion at the Kuhn scale (Sec. 5.3) and the shear relaxation modulus of unentangled melts (Sec. 5.4). At the entanglement scale, we start out with an empirical relation between for entanglement length,  $N_{eK}(\kappa)$ , which we compare to available theoretical predictions (Sec. 5.5). Next we define the entanglement time,  $\tau_e$ , as the time, when the monomer mean-square displacements of Phantom KG chains exceed the tube diameter (Sec. 5.6). Then we discuss the chain dynamics around the entanglement time (Sec. 5.7). Our central result is the demonstration, that the tube model almost quantitatively predicts the magnitude of the monomer displacements in the  $t^{1/4}$ -regime (Sec. 5.7) given the Kuhn length, PPA input for the entanglement length, and the local friction at the bead scale inferred from *oligomer* diffusion data.

### 5.1 Kuhn length

Figure 8 summarizes our results for the Kuhn length of KG chains. Our estimates are slightly but systematically higher than those reported previously, because we accounted for long-range bond orientation correlations<sup>44,45,58–60</sup> in our extrapolations to the asymptotic limit. We have performed a block analysis, which shows that the statistical error is smaller than the symbol size.

Overall, the data show the expected monotonous increase of the Kuhn length with increasing bending stiffness. Results for stiff KG chains with  $\kappa > 2$  are in excellent agreement with the expected bare Kuhn length, Eq. (8). For these systems the Flory ideality hypoth-

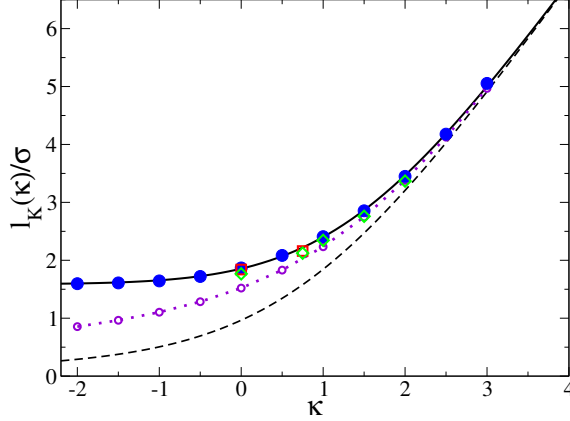


Figure 8: Extrapolated Kuhn length  $l_K$  vs stiffness parameter  $\kappa$  (blue filled circles) and our parameterization eqs. (8 and 50) (black solid line). Also shown are the local Kuhn length  $l_K^{(1)}$  (open violet circles connected by dotted line), the bare Kuhn length  $l_K^{(0)}(\kappa)$  (black dashed line), literature data from Hoy et al.<sup>101</sup> (red box) and Moreira et al.<sup>98</sup> (green diamond).

esis<sup>8</sup> holds and excluded volume interactions are completely screened. However, Eq. (8) significantly underestimates the Kuhn length of the more flexible chains.

As a first step towards taking into account excluded volume effects, we can devise a local Kuhn length estimate,  $l_K^{(1)}$ , (violet open circles and dashed lines in Fig. 8 ) by evaluating Eq. (7) using the actual distribution of bond angles sampled from our simulation data. This includes the local effects of bead packing and, in particular, effects of the excluded volume between next-nearest neighbor beads along the chain. This approximation breaks down for  $\kappa < 1$ , where pair-interactions and the correlation hole can no longer be neglected.

The large-scale statistics of the intrinsically most flexible systems are influenced by long-range bond orientation correlations<sup>44,58-60</sup> with  $l_K > l_K^{(1)} > l_K^{(0)}$ . To parameterize the Kuhn length dependence on chain stiffness we fitted the difference between the extrapolated and bare Kuhn lengths,

$$l_K(\kappa) \equiv l_K^{(0)}(\kappa) + \Delta l_K(\kappa) , \quad (49)$$

by an empirical formula

$$\frac{\Delta l_K(\kappa)}{\sigma} = 0.77 \left( \tanh \left( -0.03\kappa^2 - 0.41\kappa + 0.16 \right) + 1 \right) . \quad (50)$$

We expect this parameterization to be reasonably accurate outside the range of  $\kappa$ -values for which we have data: systems with  $\kappa > 2.5$  should be well described by eq. (8), while the effect of a stronger bias than  $\kappa < -2$  towards large bending angles will be limited by the repulsive next-nearest neighbor excluded volume interactions.

The main panel of Fig. 1 illustrates the utility (as well as the limits) of the Kuhn length for describing the single-chain statistics. While  $l_K$  properly characterizes the scale of the crossover from rigid rod to random walk behavior, the form of the crossover function is influenced by corrections to the Flory theorem, whose importance decreases with chain stiffness. A detailed analysis of the interplay between intrinsic stiffness and the effects of the incomplete screening of excluded volume effects in polymer melts<sup>44,45,51–54,58–60</sup> is beyond the scope of the present work. We will return to this point in a separate article.

## 5.2 Kuhn time and friction

Single-chain models of the polymer *dynamics* (Secs. 2.3 to 2.5) require information on the local viscosity. In Sections 4.4 and 4.5 we have inferred a surprisingly simple, stiffness- and essentially chain length independent value for the effective bead friction,  $\zeta_b = 12.4m_b\tau^{-1}$ , in KG melts, Eq. (45). Our conclusions are based on the agreement between results for KG melts and for Phantom KG chains, whose effective bending stiffness  $\tilde{\kappa}(\kappa)$  reproduces the Kuhn lengths of the target KG melts. While the accord is trivial for the initial ballistic regime at times  $t \ll m_b/\zeta_b$ , this is not at all the case around the Kuhn time, where the monomer dynamics is strongly influenced by intra- and inter-chain interactions. Our findings present a remarkable confirmation of (i) the intuition of Edwards, Freed and Muthukumar<sup>102–105</sup> that the many-chain dynamics in polymer melts may be represented by a single-chain model and (ii) the quantitative analysis of Semenov *et al.*, who found that correlation hole effects<sup>51</sup> and viscoelastic hydrodynamic interactions<sup>52–54</sup> cause negligible corrections to the *long-term* CM diffusion and the *short-term* monomer motion.

In particular, we are now in a position to evaluate the Kuhn friction, time, and viscosity,

Eqs. (24) to (26), as defined in Sec. 2.6. Using Eq. (45) for the bead friction in KG melts, these quantities can be expressed in simulation units as

$$\zeta_K(\kappa) \equiv \frac{l_K(\kappa)}{l_b} \zeta_b = 12.8 \left( \frac{l_K(\kappa)}{\sigma} \right) m_b \tau^{-1} \quad (51)$$

$$\tau_K(\kappa) \equiv \frac{1}{3\pi^2} \frac{\zeta_K(\kappa) l_K^2(\kappa)}{k_B T} = 0.434 \left( \frac{l_K(\kappa)}{\sigma} \right)^3 \tau \quad (52)$$

$$\eta_K(\kappa) \equiv \frac{1}{36} \frac{\zeta_K(\kappa)}{l_K(\kappa)} = 0.357 m_b \sigma^{-1} \tau^{-1} . \quad (53)$$

The rapid increase of  $\tau_K$  with stiffness is illustrated in Fig. 15, which summarises results for characteristic time scales of KG melts as a function of the ratio,  $\left( \frac{l_K(\kappa)}{\sigma} \right)$ , of Kuhn length and bead size. As a side remark we note, that with  $g_2(t) \propto l_K^2(t/\tau_K)^{1/2} \propto (l_K/\sigma)^{1/2}$  the variation of the monomer diffusion in the Rouse regime is much weaker.

### 5.3 Monomer motion around the Kuhn scale

Does it really make sense to *define* quantities characterising the dynamics at the Kuhn scale by using expressions from the *continuum* Rouse model? Figure 9a shows our results for the monomer diffusion of Phantom KG chains with  $N_K = 80$  from Fig. 7. Instead of individual panels representing results for different system in the “microscopic” LJ units, we now use Kuhn units to present all data in a single plot. As expected, the behavior is non-universal for times up to the Kuhn time, while the different data sets almost perfectly coincide for  $t \geq \tau_K$ .

The characteristic Rouse behavior of flexible chains (the solid orange line in Fig. 9a) is only fully developed for  $t > \mathcal{O}(100)\tau_K$ . This has consequences, when one tries to associate a time scale,  $\tau_x$ , to a known spatial scale,  $R_x$ , or chain (contour) length,  $N_x$ , through the condition,

$$g_{12}(\tau_x) \equiv a_{\tau_x} \frac{2}{\pi^{3/2}} R_x^2 \equiv a_{\tau_x} \frac{2}{\pi^{3/2}} \langle R^2(N_{xK}) \rangle , \quad (54)$$

that the monomer displacements exceed  $R_x^2$  at  $t = \tau_x$ . Eq. (54) and the prefactor  $\frac{2}{\pi^{3/2}}$  are

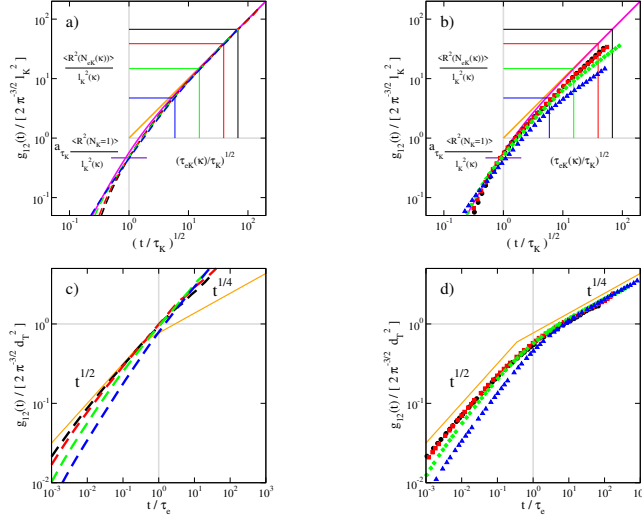


Figure 9: Monomer motion of Phantom KG chains (l.h.s column, dashed lines) and in fully interacting KG melts (symbols, r.h.s. column) plotted in Kuhn units (top row) and entanglement units (bottom row). Data in (abc) for  $N_K = 80$  systems as in Fig. 7. Data in (d) for highly entangled chains with  $N_b = 10000$  beads. Colors indicate the effective chain stiffness:  $\kappa = -1$  (black),  $\kappa = 0$  (red),  $\kappa = 1$  (green), and  $\kappa = 2$  (blue). As before, we use dashed lines to indicate results for Phantom KG chains and symbols to show data for fully interacting KG melts. The thick orange diagonal lines are parameter-free predictions from the Rouse and tube models, Eq. (36). See the main text for an explanation of the magenta line. Panel (a): Following the logic of the tube model, we estimate the entanglement time by evaluating, when the monomer mean-square displacements in the topologically *unconstrained* Phantom KG chains reach the tube diameter (Eq. (59),  $\kappa$ -dependent colored horizontal and vertical lines). Panel (b): The monomer mean-square displacements in fully interacting KG melts starts to slow down well before reaching the entanglement scale. Panel (c): In entanglement units, the motion of Phantom KG chains is *not* universal on the entanglement scale. Panel (d): Beyond the entanglement scale, the monomer mean-square displacements in fully interacting KG melts approach the prediction of the tube model.



directly motivated by the Rouse expression, Eq. (19), while  $a_{\tau_x}$  is a fudge factor, which ideally reduces to  $a_{\tau_x} = 1$ . As an example,<sup>3</sup> consider the relaxation time of subchains of length  $N_K/p$  with  $p = 2, 3, \dots$  and a mean-square end-to-end distance,  $R_p^2 = (N_K/p)l_K^2$ . Evaluating Eq. (19) for  $a_{\tau_x} = 1$  assuming Rouse dynamics, Eq. (19), yields  $\tau_p = \tau_R/p^2$ , i.e. the relaxation time of the  $p$ th Rouse mode. Inspection of Fig. 9a shows, that this procedure can be safely applied for Phantom KG (sub)chains composed of  $N_{xK} > 10$  Kuhn segments.

What happens, if one tries to push this argument to the Kuhn scale as the absolute validity limit of the Rouse and Gaussian chain model? Insisting on the Gaussian estimate  $R_K^2 = l_K^2$  entails the need to introduce a fudge factor of  $a_{\tau_K} \approx 0.5$  to recover an estimate of the Kuhn time from the  $g_2(t)$  data, which agrees with our *definition*, Eq. (25). While this is acceptable on a scaling level, we have noted a surprisingly close relation between the statics and dynamics of Phantom KG chains. Considering  $N_K$  as a continuous variable, we can invert Eq. (27) to identify the length of a chain,  $N_{1K}(t) = \sqrt{t/\tau_K}$ , whose relaxation time corresponds to a given time,  $t$ . In a second step, we rewrite Eq. (31) in the asymptotically correct form  $g_2(t) = \frac{2}{\pi^{3/2}} \langle R^2(N_{1K}(t)) \rangle$ . In the final step, we use the wormlike chain expression, Eq. (9), to estimate the consequences of chain stiffness and finite extensibility. The resulting solid magenta line in Fig. 9a is in much better agreement with the data than the asymptotic Rouse prediction. Without attempting a deeper analysis, we conclude that the Rouse relation for the equilibration length  $l_1(t)$  holds in wormlike chains already around the persistence length. The dynamics of semiflexible chains on smaller scales is described by different relations,<sup>106</sup> with inertial effects providing additional corrections in the present case. In practical terms, we can use the intercept

$$g_{12}(\tau_K^{(est)}) \equiv a_{\tau_K} \frac{2}{\pi^{3/2}} \langle R^2(N_K = 1) \rangle . \quad (55)$$

as an estimator for the Kuhn time, where  $a_{\tau_K} = 0.82$  and  $\langle R^2(N_K = 1) \rangle / l_K^2 = 0.57$  from Eq. (9). In Figure 9, the Kuhn time estimator is illustrated by the horizontal violet line.

Panel b of Figure 9 shows corresponding mean-square monomer displacement data for fully interacting chains in KG melts. Up to the Kuhn time, the results are nearly identical to those for the corresponding Phantom KG chains. As illustrated in Fig. 15, the estimates of  $\tau_K$  based on melt data and Eq. (55) are in good agreement with Eq. (52). Entanglement effects restrict the time window,  $\tau_K \ll t \ll \tau_e$ , over which the Rouse model can be expected to apply. In particular, topological constraints destroy the universality in the monomer motion beyond the Kuhn scales, because the number of Kuhn segments per entanglement length,  $N_{eK}$ , decreases with stiffness. In practice, monomer mean-square displacements in the melt never attain the asymptotic Rouse regime, Eq. (31), because entanglements significantly slow down the motion at the scale, where the corresponding Phantom KG chains start to exhibit Gaussian behavior. As a consequence, fitting the signature prediction, Eq. (19), of the Rouse model to data in this range is bound to overestimate the friction. For flexible chains ( $\kappa \leq 0$ ), the effect is weak. They show an extended effective  $t^{1/2}$  regime, albeit with an amplitude which is only about 70% of the expected value. Since  $g_2(t) \propto \sqrt{t/\tau_K}$ , corresponding estimates of  $\zeta_b$ ,  $\zeta_K$ , and  $\tau_K$  would exceed our values by a factor of two. For stiffer chains, the Rouse regime is effectively suppressed by a broad crossover from semi-flexible to entangled dynamics, rendering the extraction of a bead friction delicate.

## 5.4 Shear relaxation moduli of unentangled melts

The second signature prediction of the Rouse model is the power law decay, Eq. (32), of the shear relaxation modulus,  $G(t)$ .<sup>4</sup> In Figure 10, we show data in Kuhn units for phantom KG chains of different stiffness,  $\kappa$ , for times  $t > \tau$ , when high-frequency oscillations due to the bond length relaxation have died off.<sup>107</sup> We observe perfect data collapse for equivalent chain lengths,  $N_K$ , as well as excellent agreement with the predictions, Eq. (21), of the Rouse model.

Figure 11 presents a comparison between the Rouse model and simulation data for fully interacting KG melts with  $\kappa = -1, 0, 1, 2$ . Our results cover the crossover from unentangled

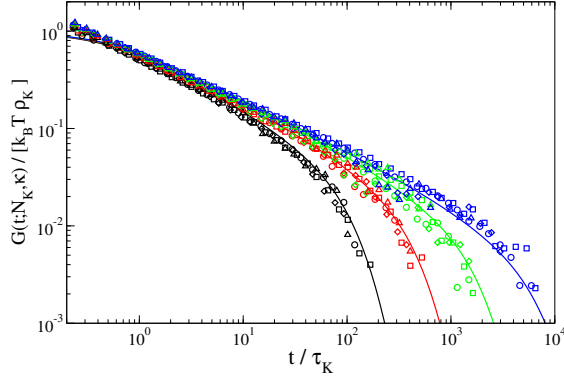


Figure 10: Shear-relaxation modulus for phantom KG melts with for stiffness  $\kappa = -1, 0, 1, 2$  (circle, box, diamond, triangle, respectively) for chain length  $N_K = 10, 20, 40, 80$  (black, red, green, blue, respectively). Shown are also the predictions of Rouse theory (lines with colours matching simulation data).

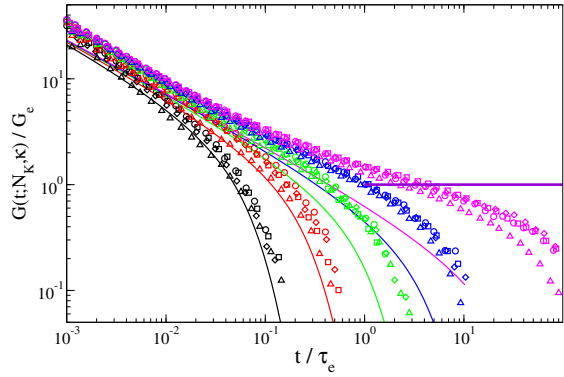


Figure 11: Shear-relaxation modulus for KG melts with chain length  $Z = 0.25, 0.5, 1, 2, 5$  (black, red, green, blue, magenta, respectively) for stiffness  $\kappa = -1, 0, 1, 2$  (circle, box, diamond, triangle, respectively) and  $N_{eK}(\kappa) = 68, 39, 15, 5.2$ . Shown are also the predictions of Rouse theory (lines with colours matching simulation data). The horizontal violet line illustrate the entanglement modulus.

to weakly entangled melts. In contrast to Fig. 10 we present the data in entanglement units to show that the terminal relaxation time is governed by the *effective* chain length,  $Z = 0.25, 0.5, 1, 2, 5$ . The observed terminal relaxation times for the shortest chains are in good agreement with the Rouse model. The weakly entangled melts show a progressively delayed decay. As expected, data for different chain lengths for a given  $\kappa$  collapse for short times. Furthermore, they are qualitatively compatible with a power law decay. However, the observed decay is somewhat steeper than predicted by the Rouse model and depends on  $\kappa$ . Likhtman *et al.*<sup>107</sup> already reported this effect for the standard ( $\kappa = 0$ ) KG model and attributed their observation to glassy relaxation modes related to bead-bead interactions, which are not accounted for in the Rouse model. This interpretation seems compatible with our finding, that the absolute stress level is systematically *above* the prediction from the Rouse model. Contrary to the monomer diffusion, the absolute magnitude of the deviation for  $G(t)$  seems to *decrease* with stiffness. Thus while there is qualitative agreement in the sense that both monomer motion and stress relaxation are slower than predicted by the Rouse model, there is little hope that both quantities could be simultaneously fitted with effective parameters.

## 5.5 Entanglement length

Our PPA results for the entanglement length in KG melts (Fig. 4) can be summarized as

$$N_{eK}(\kappa) = -0.84\kappa^4 + 3.14\kappa^3 + 3.69\kappa^2 - 30.1\kappa + 39.3 . \quad (56)$$

For the  $\kappa$ -range we have studied, the number of Kuhn segments per entanglement length decreases by a factor of 20 from  $N_{eK}(\kappa = -1) = 69$  to  $N_{eK}(\kappa = 2.5) = 3.5$ . This underlines the necessity of applying corrections to random walk theory when describing the chain statistics at the entanglement scale of stiffer polymers.

Following the packing argument,<sup>108,109</sup> the entanglement length for loosely entangled

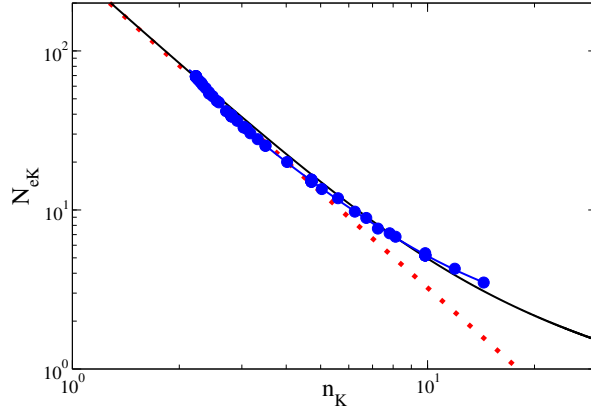


Figure 12: Number of Kuhn units between entanglements for KG models with varying stiffness (blue solid circles), empirical fit eq. (56) (thin blue line), prediction for cross-over eq. (58) (solid black line), and prediction in the flexible limit eq. (57) (red dashed line) both with  $\alpha = 18$ .

chain with  $N_{eK} \gg 1$  should be given by

$$N_{eK} = \frac{\alpha^2}{n_K^2} \quad (57)$$

where experiments<sup>110</sup> and a simple geometrical argument for binary entanglements<sup>27</sup> suggest  $\alpha = 19 \pm 2$ . The parameter  $\alpha$  can be interpreted as the number of entanglement strands per entanglement volume. Uchida *et al.*<sup>46</sup> developed a scaling theory to describe the crossover to the tightly entangled regime, suggesting instead

$$N_{eK} = x^{\frac{2}{5}} \left(1 + x^{\frac{2}{5}} + x^2\right)^{\frac{4}{5}} \quad \text{with} \quad x = \frac{\alpha}{n_K} \quad (58)$$

Fig. 12 shows the variation of the number of Kuhn segments between entanglements as function of the Kuhn number. As expected from Fig. 4 the number of Kuhn units between entanglements drops as chains become stiffer, i.e. the Kuhn number grows. We observe good agreement between all our simulation results and the prediction of the Uchida theory eq. (58). For  $n_K < 4$  the approximation for flexible chains eq. (57) is also in good agreement with our simulation data. This suggests that we could, in fact, replace our empirical formula

eq. (56) with the theoretically motivated extrapolation eq. (58). However, as can be seen from the figure, this will be less accurate description of our data for the melts with the most flexible chains.

## 5.6 Entanglement time

The primitive path analysis<sup>16</sup> promises to endow the tube model with predictive power by inferring the entanglement *length*,  $N_{eK}$ . Assuming that the Rouse-like longitudinal dynamics is governed by the same effective bead friction, we can directly read off the entanglement time from the standard relation,<sup>4</sup>  $\tau_e = N_{eK}^2 \tau_K$ . As a consistency check, we can estimate the entanglement time through the relation<sup>1</sup>

$$\lim_{N_K \rightarrow \infty} g_2^{phantom}(\tau_e^{(est)}) \equiv \frac{2}{\pi^{3/2}} \langle R^2(N_{eK}) \rangle . \quad (59)$$

where  $d_T^2 = \langle R^2(N_{eK}) \rangle$  ought to be a good approximation for the tube diameter of loosely entangled chains. Figure 9a illustrates the application of Eq. (59) to data for the monomer motion of Phantom KG chains, which we use as a reference for the dynamics of topologically *unconstrained* chains. The entanglement scale is indicated by the combination of (i) horizontal lines representing the spatial scale inferred from the primitive-path analysis and the single-chain statistics and (ii) vertical lines marking the temporal scale inferred from Eq. (59). Following the discussion in Sec. 5.3, it is not surprising that the results are in almost perfect agreement with the standard relation,  $\tau_e = N_{eK}^2 \tau_K$  (Fig. 15). Note that with  $N_{eK} \sim (\sigma/l_K)^4$  predicted by the packing argument, the ratio  $\tau_e/\tau_K \sim (\sigma/l_K)^8$  decreases extremely rapidly when considered as a function of Kuhn length.

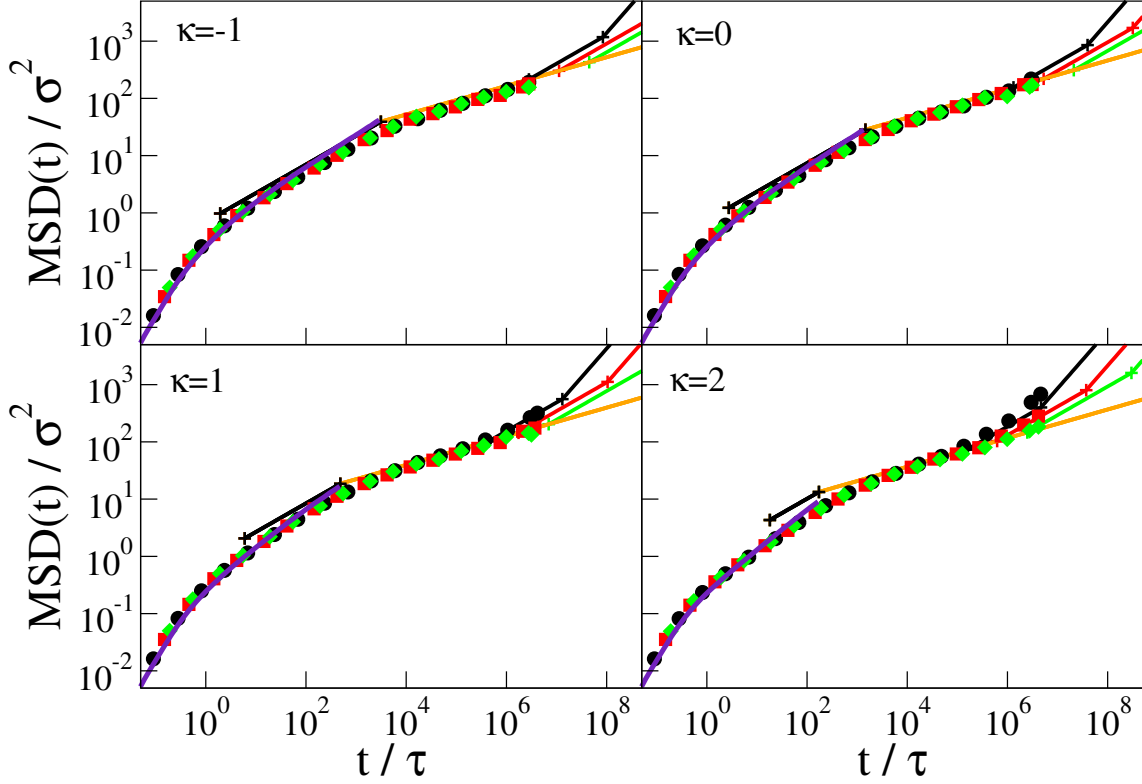


Figure 13: Monomer mean-square displacement,  $g_1(t)$ : Comparison between simulation data for KG melts and parameter-free predictions of the tube model, Eqs. (36). MSDs were sampled melts of  $Z = 10, 20, 40$  (black, red, green symbols, respectively) for the middle 25% of the chains for  $\kappa = -1, 0, 1, 2$ . + symbols denotes the cross-over times  $\tau_K, \tau_e^*, \tau_R^*$ , and  $\tau_{max}$ , respectively, for the different melts.  $g_1(t)$  sampled for the phantom KG melts is shown up to  $\tau_e^*$  (violet line).

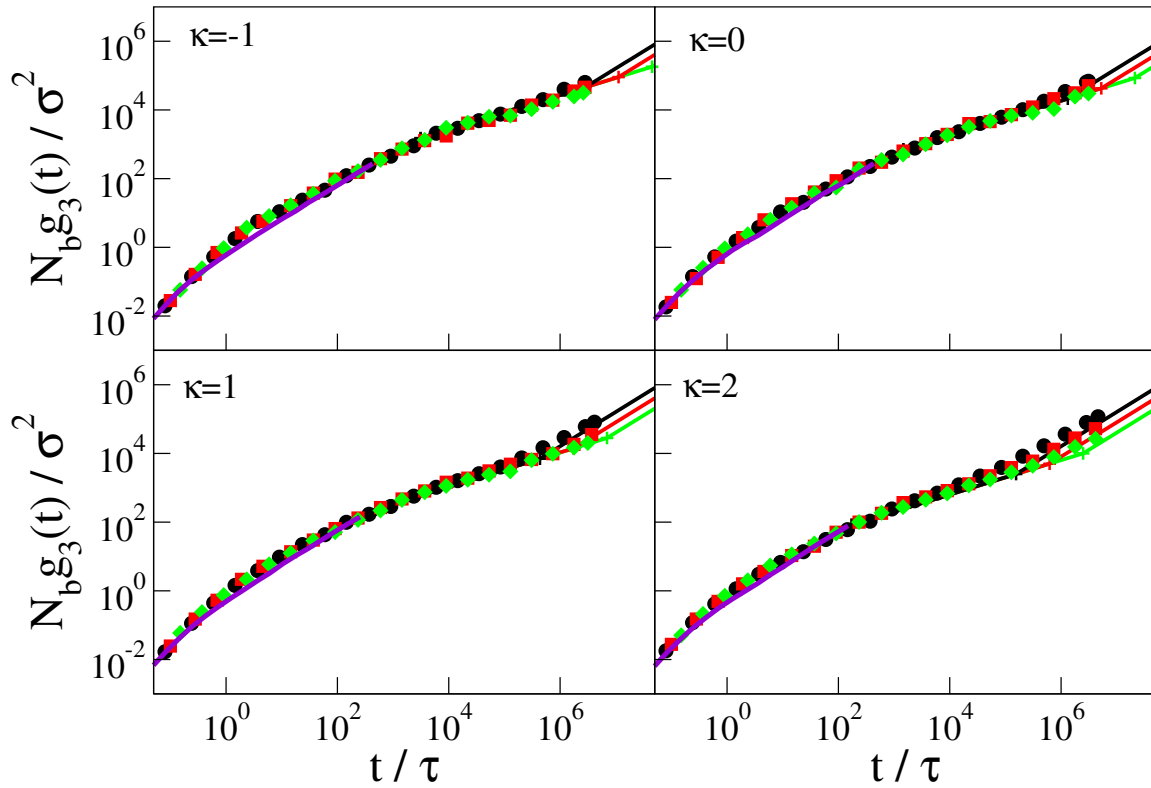


Figure 14: CM mean-square displacement,  $g_3(t)$ : Comparison between simulation data for KG melts and parameter-free predictions of the tube model, Eqs. (37). See Fig. 13 for the meaning of symbols and lines.



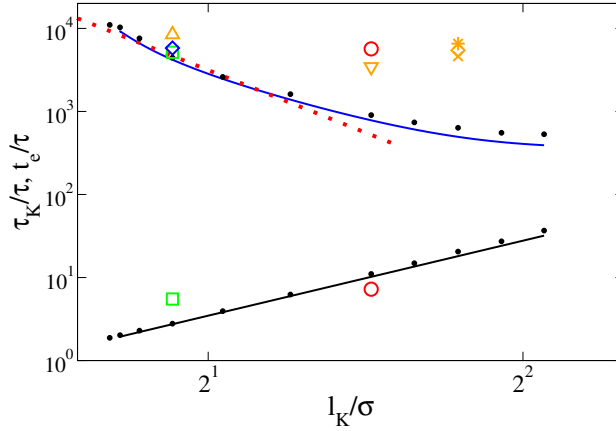


Figure 15: Characteristic times as functions of the Kuhn length. Lines denote the estimated Kuhn time using Eq. (52) (black line), estimated entanglement time  $\tau_e = \tau_K N_{eK}^2$  using Eqs. (52, 56) (blue line), and estimated using the packing entanglement length Eqs. (52, 57) (red dotted line). Small filled black circles denotes independent estimations  $\tau_K^{(est)}$  and  $\tau_e^{(est)}$  using Phantom KG simulations Eqs. (55, 59). Big colored symbols denote literature values for the Kuhn and entanglement times from Kremer and Grest<sup>19</sup> (green boxes), the entanglement time estimated by Likhtmann et al.<sup>107</sup> (blue diamond), the Kuhn and entanglement times estimated Hsu et al.<sup>71</sup> (red circles), and the entanglement times estimated by the reanalysis of cross-over positions in literature data for  $\kappa = 0$ ,<sup>112</sup>  $\kappa = 1.5$ ,<sup>71</sup> and  $\kappa = 2.0$ <sup>112-114</sup> by Hou<sup>115</sup> (orange triangle up, triangle down, cross, diamond, star, respectively). (see text for discussion)

## 5.7 Chain dynamics around the entanglement scale

Are our entanglement times, which are *predictions* based on PPA results and the dynamics of Phantom KG chains, relevant to the actual melt dynamics? A first piece of evidence is provided by the shear relaxation moduli of weakly entangled melts, Fig. 11. Figure 13 shows our results for the monomer diffusion,  $g_1(t)$ , sampled for beads in the central half of the chain in entangled KG melts with  $Z = 10, 20, 40$ . Corresponding results for the CM diffusion,  $g_3(t)$ , in the same systems are shown in Fig. 14. The data in these figures correspond to about 103 core years of simulation effort. As previously observed,<sup>19,69,71</sup> KG melts show convincing evidence for the initial  $t^{1/4}$  and  $t^{1/2}$ -regimes predicted by the tube model for the monomer and the CM motion. The key point to note here is the good quantitative agreement between our data and the predictions, Eqs. (36) and Eqs. (37), of the tube model. We emphasize, that this comparison constitutes a parameter-free test of the tube model and provides additional evidence for the power of the primitive path analysis<sup>16</sup> of the microscopic topological state. Importantly, the model provides a remarkably consistent description of the chain dynamics using a (PPA) value of  $N_{eK}$ , which has already been shown to quantitatively predict the plateau modulus of KG melts<sup>17,71</sup> and which corresponds to the experimentally defined *rheological* entanglement length.<sup>83</sup>

However, no model is perfect. In Fig. 9 we (re)plot  $g_1(t)$  in entanglement units to analyse the  $t^{1/4}$ -regime and the crossover at the entanglement scale in more detail. Panel (c) shows data for our Phantom KG reference chains. As expected from Eq. (59), all  $g_1(t)$  cross the tube scale as at  $\tau_e$  exhibiting (almost) perfect Rouse behaviour. Panel (d) shows results for highly entangled chains with  $N_b = 10000$  monomers and  $Z > 80$ , which exhibit a broad and universal  $t^{1/4}$ -regime between  $\tau_e$  and  $\tau_R = Z^2\tau_e$ , confirming once more the internal consistency of our choices for the  $\kappa$ -dependent time- and length scales. At the same time, there are notable deviations from Eq. (36).

---

<sup>1</sup>In Eq. (59) we have neglected the analogue,  $a_{\tau_e}$ , of the correction factor in Eq. (55) for the Kuhn time, because Phantom KGchains are nearly Gaussian on the entanglement scale (Fig. 9). Note that when this approximation breaks down, one also needs to reconsider the definition of the tube diameter.<sup>111</sup>

Literature values of  $\tau_e$  are typically inferred from the intercept<sup>19</sup> between an (effective)  $t^{1/2}$  Rouse regime and the  $t^{1/4}$  regime in the monomer diffusion data like those shown in Fig. 9d. Kremer and co-workers<sup>19,69,71</sup> identified  $\tau_e$  on a scaling level with the position of the crossover,  $\tau_e = \tau_e^*$ . Likhtman and McLeish<sup>70</sup> started to take into consideration prefactors and suggested  $\tau_e = (36/\pi^3)\tau_e^*$ . We subscribe to Hou’s analysis,<sup>67,115</sup>  $\tau_e = (9/\pi)\tau_e^*$ , which follows from Eq. (35). Fig. 9d points to the additional difficulty, that the crossover is not universal. Rather we encounter the mirror image of the effect discussed in Sec. 5.3: The stiffer the chains, the more  $g_1(t)$  lags behind the expectation from the continuum Rouse model, and the larger the apparent  $\tau_e^*$ .

For the standard KG model with  $\kappa = 0$ , Kremer and Grest<sup>68</sup> reported a crossover of  $\tau_e^* = 1800\tau$  in our interpretation, which corresponds to  $\tau_e = 5160\tau$  when taking the prefactors into account. Similarly, Wang et al.<sup>112</sup> reported  $\tau_e^* = 2950\tau$ , which correspond to  $\tau_e = 8450\tau$ . Finally, Likhtmann<sup>107</sup> reported  $\tau_e(\kappa = 0) \approx 5800\tau$  from a direct comparison of KG simulation data to a slip-spring model, where no prefactor corrections should be required since the slip-spring model generates the power-law regimes and cross-overs independent of theory. After taking prefactors into account, these literature results are roughly consistent, since estimating the precise cross-over position accurately is difficult. For comparison our entanglement time is estimated by combining primitive path analysis to obtain  $N_{eK}$  with our estimate of the bead friction to obtain  $\tau_e = 4200\tau$  compared to  $\tau_e^{(est)} = 4440\tau$  which is the time it takes the phantom KG mean-square displacements to reach the tube diameter.

For KG models of  $\kappa = 1.5$  and 2.0, all literature estimates shown in Fig. 15 are based on estimation of cross-over times. For  $\kappa = 1.5$ , Hsu et al. reported  $\tau_e^* = 1980\tau$  while in a reanalysis of their data Hou<sup>115</sup> estimated the cross-over at  $\tau_e^* = 1200\tau$ . This corresponds to  $\tau_e = 5670\tau$  and  $3440\tau$ , respectively. Our analysis would suggest  $\tau_e = 780\tau$  and  $\tau_e^{(est)} = 905\tau$ . For  $\kappa = 2.0$ , Hou<sup>115</sup> reanalyzed literature data<sup>112–114</sup> to find  $\tau_e^* = 1610, 1900, 2290\tau$ , respectively. This corresponds to  $\tau_e = 4610, 5440, 6560\tau$ , when taking into account the prefactor. For comparison, our analysis would suggest  $\tau_e = 490\tau$  and  $\tau_e^{(est)} = 635\tau$ . The

reported values are an order of magnitude larger than our estimates of the entanglement time.

We note that there is an order of magnitude time shift between the dynamics of the flexible and stiff KG melts shown in Fig. 9d. Hence if we fitted the theoretical prediction our simulation data we would also over estimate the entanglement times. This suggests that it is in fact impossible to use mean-square internal distances alone as a basis for estimating the entanglement time of stiff polymer melts.

As a second notable deviation, we find only about 80% of the expected value for the amplitude of the motion in the  $t^{1/4}$ -regime, Eq. (36), which in turn depends on the absolute values of our target characteristic time and length scales: Kuhn length,  $l_K$ , the number of Kuhn segments per entanglement length,  $N_{eK}$ , and the Kuhn and entanglement time,  $\tau_K$  and  $\tau_e$ . According to Eq. (35) this deviation could be explained by (i) a systematic overestimation of  $a_{pp}$  by 20% and of  $N_{eK}$  by a factor of  $1.2^2 \approx 1.4$  by the primitive path analysis, (ii) an effective bead friction for the *longitudinal* motion along the tube exceeding our estimate by a factor of  $1.2^4 \approx 2$ , or (iii) a combination of both effects. Given the excellent agreement with the measured plateau moduli,<sup>17,71</sup> (i) seems unlikely, while a comparable discrepancy between the effective bead frictions for short and long chains was already reported by Kremer and Grest<sup>19,69</sup> for the standard KG model with  $\kappa = 0$ . In our understanding,<sup>116</sup> a universal effect seems at least qualitatively conceivable, if topological constraints and the screening of hydrodynamic interactions both set in on the same scale. However, we can only speculate, if this idea could be explored in the framework of Refs.<sup>51-54</sup>

Importantly, there is also evidence to the contrary, because the effective bead friction for the longitudinal motion directly affects the expected crossover time,  $\tau_R^* = \pi\tau_R$ , from the  $t^{1/4}$  to the second  $t^{1/2}$ -regime *independently* of the tube geometry. While our data are insufficient to address this point, we note that Hsu and Kremer<sup>71</sup> reported a corresponding crossover time of  $\tau_R(N_b = 500, \kappa = 1.5) = 6.44 \times 10^5 \tau$ . Identifying their observation with  $\tau_R^*$  leads to an effective bead friction of  $\zeta_b = 8.7m_b\tau^{-1}$ . Which is also consistent with the reported cross-

over of Wang et al.<sup>112</sup> of  $\tau_R(n_b = 350, \kappa = 2) = 3.0 \times 10^5 \tau$ . Identifying their observation with  $\tau_R^*$  leads to an effective bead friction of  $\zeta_b = 6.9 m_b \tau^{-1}$ . A more accurate estimate appears to be based on directly mapping simulation results to slip-spring simulations,<sup>107,112</sup> where the prediction of tube theory Eq. (36) emerges directly from the simulation results.

## 6 Summary and Conclusion

In this paper, we have presented a detailed analysis of the behavior of Kremer-Grest<sup>18,19</sup> bead-spring polymer melts as a function of an additional wormlike local chain bending stiffness.<sup>38-40</sup> With  $-1 \leq \kappa \leq 2.5$  we have varied the stiffness parameter over the relevant range for experimentally available commodity polymer melts.<sup>43</sup> The focus of the present work lies on the characteristic time and length scales governing the melt behavior. In particular, we have (i) obtained reliable interpolations the stiffness dependence of the Kuhn length,  $l_K$ , the Kuhn friction,  $\zeta_K$ , the Kuhn time,  $\tau_K$ , the entanglement length,  $N_{eK}$ , in units of Kuhn steps, and the entanglement time,  $\tau_e$ , (ii) shown that these scales are relevant to dynamical observables of KG melts, which are independent from the static and short chain dynamic input data of our determination of the characteristic scales, and (iii) presented parameter-free tests of the Rouse and tube models of polymer dynamics for chains of different stiffness. The total numerical effort for the presented results exceeds 175 core years.

To estimate the Kuhn length and the effective friction at the bead or Kuhn scale, we have generated brute force equilibrated “gold standard” data. To obtain the Kuhn length,  $l_K$ , we analyzed the chain statistics using an estimator, which is sensitive to the slowly converging, large-range bond orientation correlations due to incompressibility effects.<sup>44,58-60</sup> To avoid finite chain length effects in the estimation of the entanglement length,  $N_{eK}$ , we have generated very large, highly entangled melts using a multi-scale equilibration method.<sup>76</sup> In one set of systems composed of 500 chains of  $N_b = 10000$  beads the number of entanglements per chains varies between  $Z > 85$  for the most flexible chains and  $Z = 570$  for the stiffest

systems. As a complement we further generated melts of flexible chains with 1000 chains with constant number of entanglements  $Z = 200$  to have highly entangled melts covering the entire range of chain stiffness. To infer  $N_{eK}$  from the primitive path mesh we used an estimator inspired by Ref.,<sup>46</sup> which accounts for the effects of finite chain stiffness. For the stiffest investigated systems, we observe small, but notable deviations from the packing prediction,  $N_{eK} \sim l_K^{-4}$  and excellent agreement with the predictions from Ref.<sup>46</sup> With respect to dynamics, we started by inferring the effective bead friction,  $\zeta_b$ , from our “gold standard” data for the long-time CM diffusion in unentangled and weakly entangled melts. The key for validating this estimate was the comparison to the dynamics of Phantom KG chains, which reproduce the stiffness-, inertia- and discretization-induced corrections to the ideal Rouse dynamics. Remarkably, our data are compatible with a chain length and stiffness *independent* value of  $\zeta_b$ . Given this value, the Kuhn and entanglement times follow directly from our definition, Eq. (25), and the standard, Rouse relation  $\tau_e = \tau_K N_{eK}^2$ . The two time scales are expected to be well separated in loosely entangled systems with  $N_{eK} \gg 1$ . However, over the experimentally relevant range of effective bending stiffness,<sup>43</sup> this gap closes rapidly:  $\tau_K \sim l_K^3$  grows quickly with the Kuhn length, while  $\tau_e = N_{eK}^2 \tau_K \sim l_K^{-5}$  in the initial packing regime.

To see, if the identified scales are relevant to the dynamics of KG melts, we have studied the shear relaxation moduli of our weakly entangled systems with  $Z = 0.25, 0.5, 1, 2, 5$  as well the chain dynamics in moderately entangled melts with  $Z = 10, 20, 40$  up to the Rouse time. In all cases, we find very good data collapse, when data for KG chains with different stiffness  $\kappa$  are represented in Kuhn or entanglement units. This validates our results for the characteristic length and time scale in KG melts on a scaling level as being coherent across the studied range of chain stiffness.

The careful characterization of model polymer systems at the Kuhn scale allows us to perform *parameter-free* tests of the predictions of the Rouse and tube models of polymer dynamics. Given data this is as simple as directly inserting the  $\kappa$ -dependent length and time

scales into the relevant text book expressions. The Rouse model<sup>62</sup> for polymer melts<sup>4</sup> seems to be a perfect example for G. Box’ aphorism,<sup>117</sup> that all models are wrong. We see effects of inertia, correlation hole and viscoelastic hydrodynamic effects.<sup>44,58–60</sup> Local liquid-like packing of the beads with remnants of glassy modes,<sup>107</sup> chain stiffness and finite extensibility. The crossover to the Gaussian behavior underlying the Rouse model is completed only for times beyond  $\mathcal{O}(100)\tau_K$ , corresponding to the Rouse time of a chain of  $N_K = \mathcal{O}(10)$  Kuhn segments. This is to be compared to the entanglement lengths,  $N_{eK} \in [4, 100]$ , and the observation that topological constraints affect the chain dynamics well below the tube scale. As a consequence, we have not found a single observable, which *quantitatively* follows the predictions of the Rouse model to an extent that would allow us to recover the bead friction from a direct fit of the theory to our data. And yet the model is extremely useful<sup>118</sup> due to its simplicity, the insight generated by its qualitatively correct description of the dynamics of unentangled polymers, and for being the starting point for systematic improvements. In particular, the model describes the longitudinal dynamics of entangled polymers within the tube, which occurs on scales, where the underlying Gaussian chain model quantitatively applies. Remarkably, the tube model almost quantitatively predicts the amplitude of the characteristic  $t^{1/4}$ -regime in the monomer diffusion given PPA input for the entanglement length and “bead frictions” essentially inferred from the center-of-mass diffusion of KG pentamers. Studies with longer runs for longer chains are required to confirm the small remaining discrepancy in the amplitude of the  $t^{1/4}$ -regime. In particular, it would be interesting to see, if this amplitude and the crossover to the subsequent reptation regime can be described with a consistent bead friction.

## Acknowledgement

The simulations in this paper were carried out using the LAMMPS molecular dynamics software.<sup>74</sup> Computation/simulation for the work described in this paper was supported by

the DeiC National HPC Center, University of Southern Denmark, Denmark.



## References

- (1) Flory, P. J. *Principles of polymer chemistry*; Cornell University Press: Ithaca N.Y, 1953.
- (2) Flory, P.; Volkenstein, M. *Statistical mechanics of chain molecules*. 1969.
- (3) de Gennes, P. G. *Scaling Concepts in Polymer Physics*; Cornell University Press: Ithaca NY, 1979.
- (4) Doi, M.; Edwards, S. F. *The Theory of Polymer Dynamics*; Clarendon: Oxford, 1986.
- (5) Rubinstein, M.; Colby, R. H. *Polymer physics*; Oxford University: New York, 2003.
- (6) Bird, R. B.; Armstrong, R. C.; Hassager, O. *Dynamics of Polymeric Liquids*; Wiley: New York, 1977; Vol. 1.
- (7) Kuhn, W. Über die Gestalt fadenförmiger Moleküle in Lösung. *Kolloid.* **1934**, *1*, 2.
- (8) Flory, P. J. The configuration of real polymer chains. *J. Chem. Phys.* **1949**, *17*, 303.
- (9) Binder, K. *Monte Carlo and Molecular Dynamics simulations in polymer science*; Oxford University Press: New York, 1995.
- (10) Padding, J.; Briels, W. Time and length scales of polymer melts studied by coarse-grained Molecular Dynamics simulations. *J. Chem. Phys.* **2002**, *117*, 925.
- (11) Müller-Plathe, F. Coarse-graining in polymer simulation: From the atomistic to the mesoscopic scale and back. *Chem. Phys. Chem.* **2002**, *3*, 754.
- (12) Tzoumanekas, C.; Theodorou, D. N. From atomistic simulations to slip-link models of entangled polymer melts: Hierarchical strategies for the prediction of rheological properties. *Curr. Opin. Solid State Mater. Sci.* **2006**, *10*, 61.

- (13) Peter, C.; Kremer, K. Multiscale simulation of soft matter systems - from the atomistic to the coarse-grained level and back. *Soft Matter* **2009**, *5*, 4357.
- (14) Peter, C.; Kremer, K. Multiscale simulation of soft matter systems. *Faraday Discuss.* **2010**, *144*, 9.
- (15) Maurel, G.; Goujon, F.; Schnell, B.; Malfreyt, P. Prediction of structural and thermomechanical properties of polymers from multiscale simulations. *RSC Adv.* **2015**, *5*, 14065.
- (16) Everaers, R.; Sukumaran, S. K.; Grest, G. S.; Svaneborg, C.; Sivasubramanian, A.; Kremer, K. Rheology and microscopic topology of entangled polymeric liquids. *Science* **2004**, *303*, 823.
- (17) Hou, J.-X.; Svaneborg, C.; Everaers, R.; Grest, G. S. Stress relaxation in entangled polymer melts. *Phys. Rev. Lett.* **2010**, *105*, 068301.
- (18) Grest, G. S.; Kremer, K. Molecular Dynamics simulation for polymers in the presence of a heat bath. *Phys. Rev. A* **1986**, *33*, 3628.
- (19) Kremer, K.; Grest, G. S. Dynamics of entangled linear polymer melts: A Molecular-Dynamics simulation. *J. Chem. Phys.* **1990**, *92*, 5057.
- (20) Grest, G. S.; Kremer, K.; Milner, S. T.; Witten, T. A. Relaxation of self-entangled many-arm star polymers. *Macromolecules* **1989**, *22*, 1904.
- (21) Grest, G. S.; Kremer, K. Statistical properties of random cross-linked rubbers. *Macromolecules* **1990**, *23*, 4994.
- (22) Duering, E. R.; Kremer, K.; Grest, G. S. Relaxation of randomly cross-linked polymer melts. *Phys. Rev. Lett.* **1991**, *67*, 3531.
- (23) Duering, E. R.; Kremer, K.; Grest, G. S. Structure and relaxation of endlinked polymer networks. *J. Chem. Phys.* **1994**, *101*, 8169.

- (24) Svaneborg, C.; Grest, G. S.; Everaers, R. Strain-dependent localization, microscopic deformations, and macroscopic normal tensions in model polymer networks. *Phys. Rev. Lett.* **2004**, *93*, 257801.
- (25) Svaneborg, C.; Everaers, R.; Grest, G. S.; Curro, J. G. Connectivity and entanglement stress contributions in strained polymer networks. *Macromolecules* **2008**, *41*, 4920.
- (26) Halverson, J. D.; Lee, W. B.; Grest, G. S.; Grosberg, A. Y.; Kremer, K. Molecular Dynamics simulation study of nonconcatenated ring polymers in a melt. I. Statics. *J. Chem. Phys.* **2011**, *134*, 204904.
- (27) Rosa, A.; Everaers, R. Ring polymers in the melt state: The physics of crumpling. *Phys. Rev. Lett.* **2014**, *112*, 118302.
- (28) Murat, M.; Grest, G. S. Polymers end-grafted onto a cylindrical surface. *Macromolecules* **1991**, *24*, 704.
- (29) Murat, M.; Grest, G. S. Interaction between grafted polymeric brushes: A Molecular Dynamics study. *Phys. Rev. Lett.* **1989**, *63*, 1074.
- (30) Grest, G. S.; Murat, M. In *Monte Carlo and Molecular Dynamics simulations in polymer science*; Binder, K., Ed.; Oxford University Press: New York, 1995; p 476.
- (31) Grest, G. S. Interfacial sliding of polymer brushes: a Molecular Dynamics simulation. *Phys. Rev. Lett.* **1996**, *76*, 4979.
- (32) Aoyagi, T.; Takimoto, J.-I.; Doi, M. Molecular Dynamics study of polymer melt confined between walls. *J. Chem. Phys.* **2001**, *115*, 552.
- (33) Gersappe, D. Molecular mechanisms of failure in polymer nanocomposites. *Phys. Rev. Lett.* **2002**, *89*, 058301.
- (34) Pierce, F.; Perahia, D.; Grest, G. S. Interdiffusion of short chain oligomers into an entangled polymer film. *Macromolecules* **2009**, *42*, 7969.

- (35) Yagyu, H.; Utsumi, T. Coarse-grained Molecular Dynamics simulation of nanofilled crosslinked rubber. *Comput. Mater. Sci.* **2009**, *46*, 286.
- (36) Sussman, D. M.; Tung, W.-S.; Winey, K. I.; Schweizer, K. S.; Riggleman, R. A. Entanglement reduction and anisotropic chain and primitive path conformations in polymer melts under thin film and cylindrical confinement. *Macromolecules* **2014**, *47*, 6462.
- (37) Ge, T.; Robbins, M. O.; Perahia, D.; Grest, G. S. Healing of polymer interfaces: Interfacial dynamics, entanglements, and strength. *Phys. Rev. E.* **2014**, *90*, 012602.
- (38) Faller, R.; Kolb, A.; Müller-Plathe, F. Local chain ordering in amorphous polymer melts: Influence of chain stiffness. *Phys. Chem. Chem. Phys.* **1999**, *1*, 2071.
- (39) Faller, R.; Müller-Plathe, F.; Heuer, A. Local reorientation dynamics of semiflexible polymers in the melt. *Macromolecules* **2000**, *33*, 6602.
- (40) Faller, R.; Müller-Plathe, F. Chain stiffness intensifies the reptation characteristics of polymer dynamics in the melt. *Chem. Phys. Chem.* **2001**, *2*, 180.
- (41) Lutz, J.-F.; Ouchi, M.; Liu, D. R.; Sawamoto, M. Sequence-controlled polymers. *Science* **2013**, *341*, 1238149.
- (42) Gody, G.; Maschmeyer, T.; Zetterlund, P. B.; Perrier, S. Rapid and quantitative one-pot synthesis of sequence-controlled polymers by radical polymerization. *Nature communications* **2013**, *4*, 2505.
- (43) Everaers, R.; Karimi-Varzaneh, H. A.; Hojdis, N.; Fleck, F.; Svaneborg, C. Kremer-Grest models for commodity polymer melts: Linking theory, experiment and simulation at the Kuhn scale. Manuscript submitted to *Macromolecules*. 2019.
- (44) Wittmer, J. P.; Meyer, H.; Baschnagel, J.; Johner, A.; Obukhov, S.; Mattioni, L.;

- Müller, M.; Semenov, A. N. Long range bond-bond correlations in dense polymer solutions. *Phys. Rev. Lett.* **2004**, *93*, 147801.
- (45) Semenov, A. N. Bond-vector correlation functions in dense polymer systems. *Macromolecules* **2010**, *43*, 9139.
- (46) Uchida, N.; Grest, G. S.; Everaers, R. Viscoelasticity and primitive path analysis of entangled polymer liquids: From F-actin to polyethylene. *J. Chem. Phys.* **2008**, *128*, 044902.
- (47) Pearson, D. S.; Fetters, L. J.; Graessley, W. W.; Ver Strate, G.; von Meerwall, E. Viscosity and self-diffusion coefficient of hydrogenated polybutadiene. *Macromolecules* **1994**, *27*, 711–719.
- (48) Fuchs, M.; Schweizer, K. S. Polymer-mode-coupling theory of finite-size-fluctuation effects in entangled solutions, melts, and gels. 1. General formulation and predictions. *Macromolecules* **1997**, *30*, 5133.
- (49) Fuchs, M.; Schweizer, K. S. Polymer-mode-coupling theory of finite-size-fluctuation effects in entangled solutions, melts, and gels. 2. Comparison with experiment. *Macromolecules* **1997**, *30*, 5156.
- (50) Lodge, T. P. Reconciliation of the molecular weight dependence of diffusion and viscosity in entangled polymers. *Physical Review Letters* **1999**, *83*, 3218.
- (51) Farago, J.; Semenov, A. N.; Meyer, H.; Wittmer, J. P.; Johner, A.; Baschnagel, J. Mode-coupling approach to polymer diffusion in an unentangled melt. I. The effect of density fluctuations. *Phys. Rev. E* **2012**, *85*, 051806.
- (52) Farago, J.; Meyer, H.; Semenov, A. N. Anomalous diffusion of a polymer chain in an unentangled melt. *Phys. Rev. Lett.* **2011**, *107*, 178301.

- (53) Farago, J.; Meyer, H.; Baschnagel, J.; Semenov, A. N. Mode-coupling approach to polymer diffusion in an unentangled melt. II. The effect of viscoelastic hydrodynamic interactions. *Phys. Rev. E* **2012**, *85*, 051807.
- (54) Farago, J.; Meyer, H.; Baschnagel, J.; Semenov, A. N. Hydrodynamic and viscoelastic effects in polymer diffusion. *J. Phys.: Condens. Matter* **2012**, *24*, 284105.
- (55) Kratky, O.; Porod, G. Röntgenuntersuchung gelöster Fadenmoleküle. *Rec. Trav. Chim.* **1949**, *68*, 1106.
- (56) Rosa, A.; Becker, N. B.; Everaers, R. Looping probabilities in model interphase chromosomes. *Biophys. J.* **2010**, *98*, 2410.
- (57) Auhl, R.; Everaers, R.; Grest, G. S.; Kremer, K.; Plimpton, S. J. Equilibration of long chain polymer melts in computer simulations. *J. Chem. Phys.* **2003**, *119*, 12718.
- (58) Wittmer, J. P.; Beckrich, P.; Johner, A.; Semenov, A. N.; Obukhov, S. P.; Meyer, H.; Baschnagel, J. Why polymer chains in a melt are not random walks. *Europhys. Lett.* **2007**, *77*, 56003.
- (59) Wittmer, J. P.; Beckrich, P.; Meyer, H.; Cavallo, A.; Johner, A.; Baschnagel, J. Intramolecular long-range correlations in polymer melts: The segmental size distribution and its moments. *Phys. Rev. E.* **2007**, *76*, 011803.
- (60) Beckrich, P.; Johner, A.; Semenov, A. N.; Obukhov, S. P.; Benoit, H.; Wittmer, J. P. Intramolecular form factor in dense polymer systems: Systematic deviations from the Debye formula. *Macromolecules* **2007**, *40*, 3805.
- (61) Kirkwood, J. G. Statistical mechanics of fluid mixtures. *J. Chem. Phys.* **1935**, *3*, 300.
- (62) Rouse, P. E. A theory of the linear viscoelastic properties of dilute solutions of coiling polymers. *J. Chem. Phys.* **1953**, *21*, 1272.

- (63) Edwards, S. F. Statistical mechanics with topological constraints: I. *Proc. Phys. Soc.* **1967**, *91*, 513.
- (64) de Gennes, P. G. Reptation of a polymer chain in the presense of fixed obstacles. *J. Chem. Phys.* **1971**, *55*, 572.
- (65) Khokhlov, A.; Nechaev, S. Polymer chain in an array of obstacles. *Phys. Lett.* **1985**, *112A*, 156.
- (66) Morse, D. C. Viscoelasticity of concentrated isotropic solutions of semiflexible polymers. 1. Model and stress tensor. *Macromolecules* **1998**, *31*, 7030.
- (67) Hou, J.-X. Note: Determine entanglement length through monomer mean-square displacement. *J. Chem. Phys.* **2017**, *146*, 026101.
- (68) Kremer, K.; Grest, G. S. Dynamics of entangled linear polymer melts: A Molecular Dynamics simulation. *J. Chem. Phys.* **1990**, *92*, 5057.
- (69) Pütz, M.; Kremer, K.; Grest, G. S. What is the entanglement length in a polymer melt? *Europhys. Lett.* **2000**, *49*, 735.
- (70) Likhtman, A. E.; McLeish, T. C. Quantitative theory for linear dynamics of linear entangled polymers. *Macromolecules* **2002**, *35*, 6332.
- (71) Hsu, H.-P.; Kremer, K. Static and dynamic properties of large polymer melts in equilibrium. *J. Chem. Phys.* **2016**, *144*, 154907.
- (72) Grønbech-Jensen, N.; Farago, O. A simple and effective Verlet-type algorithm for simulating Langevin dynamics. *Mol. Phys.* **2013**, *111*, 983.
- (73) Grønbech-Jensen, N.; Hayre, N. R.; Farago, O. Application of the G-JF discrete-time thermostat for fast and accurate molecular simulations. *Comp. Phys. Comm.* **2014**, *185*, 524.

- (74) Plimpton, S. Fast parallel algorithms for short-range Molecular Dynamics. *J. Comput. Phys.* **1995**, *117*, 1.
- (75) Ramirez, J.; Sukumaran, S. K.; Vorselaars, B.; Likhtman, A. E. Efficient on the fly calculation of time correlation functions in computer simulations. *J. Chem. Phys.* **2010**, *133*, 154103.
- (76) Svaneborg, C.; Karimi-Varzaneh, H. A.; Hojdis, N.; Fleck, F.; Everaers, R. Multiscale approach to equilibrating model polymer melts. *Phys. Rev. E* **2016**, *94*, 032502.
- (77) Karayiannis, N. C.; Mavrantzas, V. G.; Theodorou, D. N. A novel Monte Carlo scheme for the rapid equilibration of atomistic model polymer systems of precisely defined molecular architecture. *Phys. Rev. Lett.* **2002**, *88*, 105503.
- (78) Karayiannis, N. C.; Giannousaki, A. E.; Mavrantzas, V. G.; Theodorou, D. N. Atomistic Monte Carlo simulation of strictly monodisperse long polyethylene melts through a generalized chain bridging algorithm. *J. Chem. Phys.* **2002**, *117*, 5465.
- (79) Sides, S. W.; Grest, G. S.; Stevens, M. J.; Plimpton, S. J. Effect of end-tethered polymers on surface adhesion of glassy polymers. *J. Polym. Sci., Part B: Polym. Phys.* **2004**, *42*, 199.
- (80) Everaers, R.; Sukumaran, S. K.; Grest, G. S.; Svaneborg, C.; Sivasubramanian, A.; Kremer, K. Rheology and microscopic topology of entangled polymeric liquids. *Science* **2004**, *303*, 823.
- (81) Edwards, S. F. The statistical mechanics of polymerized material. *Proc. Phys. Soc.* **1967**, *92*, 9.
- (82) Rubinstein, M.; Helfand, E. Statistics of the entanglement of polymers: Concentration effects. *J. Chem. Phys.* **1985**, *82*, 2477.



- (83) Everaers, R. Topological versus rheological entanglement length in primitive-path analysis protocols, tube models, and slip-link models. *Phys. Rev. E* **2012**, *86*, 022801.
- (84) Hoy, R. S.; Foteinopoulou, K.; Kröger, M. Topological analysis of polymeric melts: Chain-length effects and fast-converging estimators for entanglement length. *Phys. Rev. E* **2009**, *80*, 031803.
- (85) Semenov, A. N. Dynamics of concentrated solutions of rigid-chain polymers. Part 1. Brownian motion of persistent macromolecules in isotropic solution. *J. Chem. Soc., Faraday Trans.* **1986**, *82*, 317.
- (86) Morse, D. C. Tube diameter in tightly entangled solutions of semiflexible polymers. *Phys. Rev. E* **2001**, *63*, 031502.
- (87) Kolinski, A.; Skolnick, J.; Yaris, R. Does reptation describe the dynamics of entangled, finite length polymer systems? A model simulation. *J. Chem. Phys.* **1987**, *86*, 1567.
- (88) Binder, K.; Paul, W. Monte Carlo simulations of polymer dynamics: Recent advances. *J. Polym. Sci., Part B: Polym. Phys.* **1997**, *35*, 1.
- (89) Smith, G.; Paul, W.; Monkenbusch, M.; Richter, D. A comparison of neutron scattering studies and computer simulations of polymer melts. *Chem. Phys.* **2000**, *261*, 61.
- (90) Padding, J.; Briels, W. J. Zero-shear stress relaxation and long time dynamics of a linear polyethylene melt: A test of Rouse theory. *J. Chem. Phys.* **2001**, *114*, 8685.
- (91) Kreer, T.; Baschnagel, J.; Müller, M.; Binder, K. Monte Carlo simulation of long chain polymer melts: Crossover from Rouse to reptation dynamics. *Macromolecules* **2001**, *34*, 1105.
- (92) Doxastakis, M.; Theodorou, D.; Fytas, G.; Kremer, F.; Faller, R.; Müller-Plathe, F.;

- Hadjichristidis, N. Chain and local dynamics of polyisoprene as probed by experiments and computer simulations. *J. Chem. Phys.* **2003**, *119*, 6883.
- (93) Paul, W.; Smith, G. D. Structure and dynamics of amorphous polymers: Computer simulations compared to experiment and theory. *Rep. Prog. Phys.* **2004**, *67*, 1117.
- (94) Brodeck, M.; Alvarez, F.; Arbe, A.; Juranyi, F.; Unruh, T.; Holderer, O.; Colmenero, J.; Richter, D. Study of the dynamics of poly (ethylene oxide) by combining Molecular Dynamic simulations and neutron scattering experiments. *J. Chem. Phys.* **2009**, *130*, 094908.
- (95) Abou Elfadl, A.; Kahlau, R.; Herrmann, A.; Novikov, V.; Rossler, E. From rouse to fully established entanglement dynamics: study of polyisoprene by dielectric spectroscopy. *Macromolecules* **2010**, *43*, 3340.
- (96) Colby, R. H.; Fetters, L. J.; Graessley, W. W. The melt viscosity-molecular weight relationship for linear polymers. *Macromolecules* **1987**, *20*, 2226.
- (97) Hoy, R. S.; Foteinopoulou, K.; Kröger, M. Topological analysis of polymeric melts: Chain-length effects and fast-converging estimators for entanglement length. *Phys. Rev. E.* **2009**, *80*, 031803.
- (98) Moreira, L. A.; Zhang, G.; Müller, F.; Stuehn, T.; Kremer, K. Direct equilibration and characterization of polymer melts for computer simulations. *Macromol. Theory Simul.* **2015**, *24*, 419.
- (99) Sukumaran, S. K.; Grest, G. S.; Kremer, K.; Everaers, R. Identifying the primitive path mesh in entangled polymer liquids. *J. Polym. Sci., Part B: Polym. Phys.* **2005**, *43*, 917.
- (100) Bulacu, M.; van der Giessen, E. Effect of bending and torsion rigidity on self-diffusion in polymer melts: A molecular-dynamics study. *J. Chem. Phys.* **2005**, *123*, 114901.

- (101) Hoy, R. S.; Robbins, M. O. Effect of equilibration on primitive path analyses of entangled polymers. *Phys. Rev. E* **2005**, *72*, 061802.
- (102) Edwards, S. F.; Freed, K. F. Theory of the dynamical viscosity of polymer solutions. *J. Chem. Phys.* **1974**, *61*, 1189.
- (103) Freed, K. F.; Edwards, S. Polymer viscosity in concentrated solutions. *J. Chem. Phys.* **1974**, *61*, 3626.
- (104) Freed, K. In *Progress in Liquid Physics*; Croxton, C., Ed.; Wiley, 1978; p 343.
- (105) Muthukumar, M.; Freed, K. F. Huggins coefficient for polymer solutions with excluded volume. *Macromolecules* **1977**, *10*, 899–906.
- (106) Everaers, R.; Jülicher, F.; Ajdari, A.; Maggs, A. Dynamic fluctuations of semiflexible filaments. *Phys. Rev. Lett.* **1999**, *82*, 3717.
- (107) Likhtman, A. E.; Sukumaran, S. K.; Ramirez, J. Linear viscoelasticity from molecular dynamics simulation of entangled polymers. *Macromolecules* **2007**, *40*, 6748.
- (108) Lin, Y.-H. Number of entanglement strands per cubed tube diameter, a fundamental aspect of topological universality in polymer viscoelasticity. *Macromolecules* **1987**, *20*, 3080.
- (109) Kavassalis, T. A.; Noolandi, J. New view of entanglements in dense polymer systems. *Phys. Rev. Lett.* **1987**, *59*, 2674.
- (110) Fetters, L. J.; Lohse, D. J.; Richter, D.; Witten, T. A.; Zirkel, A. Connection between polymer molecular weight, density, chain dimensions, and melt viscoelastic properties. *Macromolecules* **1994**, *27*, 4639.
- (111) Odijk, T. The statistics and dynamics of confined or entangled stiff polymers. *Macromolecules* **1983**, *16*, 1340–1344.

- (112) Wang, Z.; Likhtman, A. E.; Larson, R. G. Segmental dynamics in entangled linear polymer melts. *Macromolecules* **2012**, *45*, 3557–3570.
- (113) Zhou, Q.; Larson, R. G. Direct calculation of the tube potential confining entangled polymers. *Macromolecules* **2006**, *39*, 6737–6743.
- (114) Wang, Z.; Larson, R. G. Constraint release in entangled binary blends of linear polymers: A molecular dynamics study. *Macromolecules* **2008**, *41*, 4945–4960.
- (115) Hou, J.-X. Determine Mesh Size through Monomer Mean-Square Displacement. *Polymers* **2019**, *11*, 1405.
- (116) Ahlrichs, P.; Everaers, R.; Dünweg, B. Screening of hydrodynamic interactions in semidilute polymer solutions: A computer simulation study. *Phys. Rev. E* **2001**, *64*, 040501.
- (117) Box, G. E. P. Science and Statistics. *J. Am. Stat. Assoc.* **1976**, *71*, 791.
- (118) Box, G. E. P. *Robustness in statistics*; Elsevier, 1979; p 201.